

PARAMETRIC LEVEL-SETS ENHANCED TO IMPROVE RECONSTRUCTION (PALENTIR)*

EGE OZSAR, MISHA KILMER, ERIC MILLER, ERIC DE STURLER, ARVIND K. SAIBABA

Abstract. For inverse problems where one is concerned with recovering the shape and contrast of an unknown number of objects embedded in a medium, parametric level-set (PaLS) methods provide much of the flexibility of traditional level-set methods while avoiding many of the difficulties such as regularization and re-initialization. In this paper, we consider the restoration and reconstruction of piecewise constant objects in two and three spatial dimensions using PaLEnTIR, a significantly enhanced PaLS model relative to the current state-of-the-art. The primary contribution of this paper is a new PaLS formulation which requires only a single level-set function to recover a scene with piecewise constant objects possessing multiple unknown contrasts. Our model offers distinct advantages over current approaches to the multi-contrast, multi-object problem, all of which require multiple level-sets and explicit estimation of the contrast magnitudes. Given upper and lower bounds on the contrast, our approach is able to recover objects with any distribution of contrasts and eliminates the need to know either the number of contrasts in a given scene or their values. We provide an iterative process for finding these space-varying contrast limits. Relative to most PaLS methods which employ radial basis functions (RBFs), our model makes use of anisotropic basis functions (ABFs), thereby expanding the class of shapes that a PaLS model of a given complexity can approximate. Finally, PaLEnTIR improves the conditioning of the Jacobian matrix required as part of the parameter identification process and consequently accelerates the optimization methods by controlling the magnitude of the PaLS expansion coefficients, fixing the centers of the basis functions, and with the uniqueness of parametric to image mappings provided by the new parameterization. We demonstrate the performance of the new approach using both 2D and 3D variants of X-ray computed tomography, diffuse optical tomography (DOT), denoising, and deconvolution problems. Application to experimental sparse CT data and simulated data with different types of randomness are performed to further validate the proposed method.

Key words. level-set, PaLS, parametric, reconstruction, tomography, piecewise constant

AMS subject classifications. 65F22, 65F99, 65N21

1. Introduction. Inverse problems are of significant interest across a broad range of science and engineering applications. The primary objective of an inverse problem is to extract the unknown composition and structure of a medium based on a set of indirect observations which are related to the unknown via a physical model. In many cases, a detailed map of the medium is either not possible or not needed. Rather, one seeks the identification and characterization of “regions of interest” (ROIs), such as an cancerous tumors from diffuse optical data [5, 71, 79], subsurface contaminants from hydrological data [3, 26, 78] or buried objects from electromagnetic data [15, 18, 54, 58]. These problems are often solved by first forming an image and then post-processing to identify the ROIs [59]. Although this two-step approach can be

*This research was supported by the U.S. National Science Foundation under awards 1720291, 1935555, 1934553, 1720398, and 1720305.

effective, it is computationally expensive. Moreover, for problems where data are limited, the initial image formation stage will require potentially complex regularization methods to overcome the ill-posed nature of these problems. Alternatively one can use the data to directly estimate the geometry and contrasts of the ROIs [16, 40, 42]. These *shape-based* methods are usually better-posed compared to pixel-based problems; however, topologically complicated and discontinuous shapes can lead to challenges [63]. For example, approaches based on using parametric shapes (circles, ellipsoids, etc.) to describe object geometry require that the number of components for the shape should be *a priori* known or somehow estimated. For this and many other reasons [2], level-set methods have found great use for shape-based inverse problems because of their ability to naturally recover objects whose topology (number of connected components) is not known *a priori*.

Level-sets methods were first introduced for modeling the propagation of curves by Osher and Sethian [56]. The use of these models for solving inverse problems was initially proposed by Santosa [63] followed by significant subsequent effort based on classical level-set evolution methods [9, 22, 29, 41], most notably for image processing applications [14, 62, 72]. For ill-posed inverse problems regularization of the level-set function is required. A number of techniques have been considered to address this complication including conventional pixel-based methods [21], geometric constraints [57] or by choosing the level-set functions to be members of finite-dimensional spaces of basis functions such as the parametric level-set function (PaLS) idea, which was considered for inverse problems first by [2]. This latter approach is the basis for the work in this paper.

The PaLS model has proven to be capable of capturing the topological advantages of a level-set function while avoiding difficulties such as the need for explicit regularization and reinitialization that occur frequently when using traditional level-set methods for inverse problems. Moreover, it was shown in [2] that the low order representation of the inverse problem makes it possible to use Newton and quasi-Newton methods for determining the PaLS parameters. In recent work, the PaLS model in [2] and variants have been used across a range of application areas and imaging modalities including geophysics [51, 52] and reservoir monitoring [33, 34], image segmentation [53], acoustic scattering [19], dynamic tomography [55], dual-energy computed tomography [64], electrical impedance tomography [48, 49], electromagnetic imaging [35], electrical capacitance tomography [46], and multi-modal imaging [24].

Despite the advantages of PaLS, there remains a number of areas where improvement is required. One important limitation of existing PaLS models (indeed most all level-set methods) is the ability to recover distributions of objects with multiple contrast values. Existing level-set based approaches for multi-contrast, multi-object problems, such as the colour level-set [32], vector level-set [80], and binary level-set [47], either use N level-sets for N objects [11, 53, 80] or $\lceil \log_2 N \rceil$ level-sets for N objects [32, 47, 73]. As a result, with the existing methods, as the number of objects with different contrast values increases, the required number of level-sets also increases. A second area of limitation for PaLS concerns the family of basis functions used to model the level-set function. In a traditional PaLS setting, the level-set function is obtained using a weighted superposition of a set of predetermined collection of basis functions, most often radial basis functions (RBFs) [19, 35, 46, 48, 49, 55, 64] but also polynomials [39], multiquadrics [53], ellipsoidal [24], and polytopes [53]. We focus here on RBFs due to their prevalence. RBFs possess only circular cross sections and thus can limit the range of objects that can be represented by the model and a given number of RBFs. Finally, as effective as they are, most of the existing PaLS

models still suffer from numerical conditioning issues [2]. PaLS models which adopt RBFs can experience non-uniqueness of parametric representation of shapes due to the fact that infinitely many pairs of parameters can give the same circular cross sections. This defect can yield poorly conditioned, if not singular, Jacobian matrices, as we illustrate empirically in this paper. Since the performance of quasi-Newton methods tends to be highly dependent on the condition number of the Jacobian matrix at each iteration, most of the existing PaLS models using these methods suffer from ill-conditioning of the Jacobian matrices [2].

In this paper, we develop Parametric Level-Sets Enhanced to Improve Reconstruction (PaLEnTIR) for piecewise constant image reconstruction to address the issues identified in the above paragraph. We categorize the specific contributions and the features as follows:

- **Multi-contrast:** Most importantly, we replace the binary Heaviside function used in the existing PaLS models with a smooth transition function. This way, the new model can capture multiple unknown contrasts with only a single level-set function. To the best of our knowledge, the proposed approach is the first PaLS model that is capable of producing multiple objects each possessing different contrast values with a single level-set function. The benefit of this aspect of our model is that the number of parameters to be learned does not change when we want to produce multi-contrast images unless the number of basis functions increases. Moreover, our model does not require the explicit estimation of the contrast coefficient parameters. Rather we demonstrate the ability to determine these quantities automatically based on upper and lower bounds on the contrasts over a coarse spatial partition of the imaging region. An iterative process is provided for determining these bounds and the geometric parameters of the PaLS model.
- **Shape expressiveness:** We replace the RBFs used in previous PaLS [2] with anisotropic basis functions which yields basis functions that are capable of producing rotated ellipsoidal cross-sections. As a result, the new basis functions provide greater geometric flexibility and capture much more detail especially for sharp or flat and long objects with which RBFs have difficulty. Consequently, the new model is capable of recovering more complex objects with fewer basis functions compared to the previous model which use RBFs.
- **Numerical Behavior:** We demonstrate empirically that our new approach of bounding the coefficients used in the ABFs of the PaLS function in addition to fixing the centers of the basis functions in our new model significantly improves the numerical performance of the method. Specifically, due to these updates as well as the uniqueness of parametric representation of shapes with the use of ABFs, the condition number of the Jacobian matrices is seen to decrease and the convergence of the optimization method for estimating the PaLS parameters is observed to increase.

The organization of the paper is as follows. In section 2, we define our problem of interest and briefly review the previous parametric level-set method [2] for shape-based problems. In section 3, PaLEnTIR formulations for both 2D and 3D inverse problems are detailed. We also discuss the benefits of the new formulation relative to existing PaLS models. Our iterative approach for determining the bounds on the contrasts of the ROIs is given in section 3.1. We provide experimental results for PaLEnTIR in section 4. Specifically, from section 4.1 to 4.3, we show the results for a collection of linear 2D problems including denoising, deconvolution, inversion of the Radon transform. In section 4.4, we demonstrate the performance of PaLEnTIR on

a 3D limited view parallel beam tomography experiment. To test our approach on a nonlinear problem, we show the experimental results of the new approach on diffuse optical tomography (DOT), a nonlinear inverse problem, in section 4.5. Across this range of experiments, we use both real and synthetic data and consider different types of noise such as additive and multiplicative noise as well as data following Poisson statistics to show the robustness of our approach in a range of data-limited applications. Conclusions are provided in section 5.

2. Problem formulation. We begin by reviewing both inverse problems in general as well as the original formulation of the PaLS model.

2.1. Forward and Inverse Problems. Consider a region of space to be imaged defined as $\Omega \subset \mathbb{R}^d$, where d , the number of spatial dimensions, is either 2 or 3. For \mathbf{r} a point in Ω , let us define a spatially-dependent property $f(\mathbf{r})$ of the medium (e.g., electrical conductivity, optical absorption, sound speed, etc.). We denote with \mathcal{M} the map which takes $f(\mathbf{r})$ to a vector of noise free data. In many cases, \mathcal{M} encompasses the physics of the sensing modality as well as the engineering details of the particular sensors used to collect the data. In section 4 we detail the models underlying our examples. In practice, the data available for processing is equal to $\mathcal{M}(f)$ corrupted in some manner by noise. Unless specified otherwise, we assume that the noise is additive Gaussian. In summary, the forward model can be written

$$(2.1) \quad \mathbf{d} = \mathcal{M}(f(\mathbf{r})) + \mathbf{w},$$

where $\mathbf{w} \in \mathbb{R}^N$ represents the additive noise.

The inverse problem requires determination of the unknown function f based on the observed data \mathbf{d} . Following the penalized likelihood approach, (2.1) leads to the following minimization problem as the basis for recovering $f(\mathbf{r})$ from \mathbf{d} ,

$$(2.2) \quad \min_f \frac{1}{2} \|\mathcal{M}(f) - \mathbf{d}\|_2^2 + \xi(f).$$

The first term $\frac{1}{2} \|\mathcal{M}(f) - \mathbf{d}\|_2^2$ arises from a Gaussian assumption on the noise and quantifies the mismatch error between model prediction and the data. The second term $\xi(f)$ is the regularization functional which incorporate prior information into the minimization problem and imposes a cost on the objective function. This latter term is usually used when the problem is ill-posed and should be chosen based on properties of the problem and prior knowledge concerning e.g., the degree of smoothness associated with f [1, 25, 69]. It is also possible to regularize the problem using a geometric parameterization of the unknown property. This is done by either embedding the regularization implicitly in the parameterization of the unknown property in which case no explicit ξ may be needed or by expressing as geometric constraints on the shape of the unknown [22, 75]. In this paper, we follow the former approach using a PaLS type of model.

2.2. Parametric Level-set methods. For the problems of interest, $f \in \mathbb{R}^d \rightarrow \mathbb{R}$ consists of two types of regions; object, O , and background, $\Omega \setminus O$ and is written as

$$(2.3) \quad f(\mathbf{r}) = f_O(\mathbf{r})\chi_O(\mathbf{r}) + f_B(\mathbf{r})(1 - \chi_O(\mathbf{r}))$$

where $f_O(\mathbf{r})$ and $f_B(\mathbf{r})$ are the generally spatially dependent property values of the object and background respectively and $\chi_O(\mathbf{r})$ is the characteristic function of the

region O :

$$\chi_O(\mathbf{r}) = \begin{cases} 1 & \mathbf{r} \in O \\ 0 & \mathbf{r} \in \Omega \setminus O. \end{cases}$$

Under this model, the problem is to find O (or in some cases, the boundary, ∂O), as well as the property values in each region. A common simplifying assumption is that both f_O and f_B are constants [68] in which case the focus of the problem is on the recovery of O which in general can be multiply connected with each component having no specific (i.e., easily parameterized) shape. Due to the complicated topology of O , level-set methods have proven convenient [2]. Mathematically, the level-set representation of the shape of the domain O satisfies

$$(2.4) \quad \phi_O(\mathbf{r}) \begin{cases} < c & \mathbf{r} \in O \\ = c & \mathbf{r} \in \partial O \\ > c & \mathbf{r} \in \Omega \setminus O \end{cases}$$

where c is a constant that determines the desired level-set¹ and ∂O is the boundary of the region [2]. In terms of ϕ_O , the characteristic function of O is written as $\chi_O(\mathbf{r}) = H(\phi_O(\mathbf{r}) - c)$ where $H(x)$ is the Heaviside function which is equal to 1 for x positive, 0 for x negative and $1/2$ for $x = 0$. Thus, (2.3) can be expressed as

$$(2.5) \quad f(\mathbf{r}) = f_O H(\phi_O(\mathbf{r}) - c) + f_B (1 - H(\phi_O(\mathbf{r}) - c))$$

where f_O and f_B are the now constant property values of the foreground and background respectively.

Most of the traditional methods follows a finite difference discretization of the level-set function which requires a dense collection of nodes. The difficulty of implementing this approach as well as the numerical considerations of discrete computation overshadow the advantages of the level-set function especially in the case of ill-posed inverse problems [2, 9]. Alternatively, a parametric form for the level-set function can be used for which $\phi_O(\mathbf{r})$ is spanned by a set of basis functions (e.g., polynomial, radial basis function, trigonometric, etc). Specifically, the original parametric level-set function representation takes the form

$$(2.6) \quad \phi_{\text{rbf}}(\mathbf{r}; \mathbf{p}) = \sum_{j=1}^N \alpha_j \psi(\beta_j(\mathbf{r} - \boldsymbol{\chi}_j)), \quad \mathbf{p}^T := [\boldsymbol{\alpha}^T \ \boldsymbol{\beta}^T \ \boldsymbol{\chi}^T].$$

In this case the PaLS level-set function is formed as a weighted summation of N basis functions $\psi_j(\mathbf{r}) := \psi(\beta_j(\mathbf{r} - \boldsymbol{\chi}_j))$ for $j = 1, 2, \dots, N$. The basis functions $\psi_j(\mathbf{r})$ are often taken to be RBFs [19, 24, 35, 46, 48, 49, 55, 64]. We will refer to use of such basis functions as “RBF PaLS” and it is against such representations that we compare our new PaLEnTIR representation.² Each basis function $\psi_j(\mathbf{r})$ is associated with its own dilation coefficient β_j , and center location $\boldsymbol{\chi}_j$. The vector \mathbf{p} contains the unknowns to

¹This could be taken to be the zero level-set, though in [2], the case was made for c slightly larger.

²In the paper [2] in which the term “PaLS” was coined, the norm in the argument is replaced by a pseudo-norm and $\psi(\cdot)$ is taken to be a compactly supported radial basis function. Subsequent papers (e.g., [24]) have also built on CSRBF-based PaLS in the context of image reconstruction. The compactness of the basis functions may be advantageous from the point of view that the Jacobian may become sparse, for reasons described in [2]. The basis functions are similar in shape, representing symmetrical spherical bump functions. In the present work, however, we will use Gaussian RBFs

be determined, including the vectors α , β , and χ containing the expansion coefficients α_j , the dilation values β_j , and PaLS centers $\chi_j \in \mathbb{R}^2$ or $\in \mathbb{R}^3$ respectively. In general, the length of this vector is $(d+2)N$ which results in length $4N$ (for 2D problems) or $5N$ (for 3D).

Combining (2.6) with (2.5), we obtain $f = f(\mathbf{r}; \mathbf{p})$. The goal of a PaLS-based inverse problem is to recover the unknown \mathbf{p} based on the observed data \mathbf{d} and the known physical model \mathcal{M} . In practice, this requires replacing the exact Heaviside function with a differentiable approximation (we discuss this more in section 3.1). If the contrast coefficients f_O and f_B are known, the resultant inverse problem formulation using PaLS takes the form where $\hat{\mathbf{p}}$ solves the optimization problem

$$(2.7) \quad \min_{\mathbf{p}} \frac{1}{2} \|\mathcal{M}(f(\mathbf{r}; \mathbf{p})) - \mathbf{d}\|_2^2.$$

In the event where the contrasts are not known, a cyclic descent method is often employed [23, 29, 74] in which one alternatively estimates \mathbf{p} for using current estimates of f_O and f_B and then updates the contrasts using the just-computed PaLS parameters. A closed form expressions can be used for the latter problem, the bulk of the algorithmic effort is devoted to estimation of \mathbf{p} . This is a non-linear least squares optimization problem. We discuss how to solve the contrast problem in section 3.1.

Note that the PaLS parameterization gave us the ability to remove the regularization functional $\xi(f)$. This is due to the fact that we have regularized the problem through the parameterization as the number of PaLS basis functions is always much smaller than the size of the grid obtained from discretizing Ω .

3. Parametric Level-sets Enhanced To Improve Reconstruction. In section 2, we defined the problem using the original PaLS representation shown in (2.6). In this section, we introduce our new PaLS model, called PaLEnTIR, and we discuss its advantages over the original representation. The proposed PaLEnTIR model is defined as follows

$$(3.1) \quad f(\mathbf{r}; \mathbf{p}, C_H, C_L) = C_H T_w(\phi(\mathbf{r}; \mathbf{p}) - c) + C_L (1 - T_w(\phi(\mathbf{r}; \mathbf{p}) - c))$$

$$(3.2) \quad \phi(\mathbf{r}; \mathbf{p}) = \sum_{j=1}^N \sigma_h(\alpha_j) \psi(\mathbf{R}_j(\mathbf{r} - \chi_j)) \quad \mathbf{p}^T := [\alpha^T \beta^T \gamma^T]$$

where, as explained shortly, the N matrices $\mathbf{R}_j := \mathbf{R}(\beta_j, \gamma_j)$ for $j = 1, 2, \dots, N$ each depend on subvectors of β and γ respectively. Comparing (2.6) and (3.2), the PaLEnTIR model differs from the original PaLS method in a number of ways designed to address the shortcomings of the original approach to parametric level-sets, each of which is discussed in depth in the following sections:

1. **Multi-contrast, single level-set** reconstructions are obtained by:

- (a) Replacing the Heaviside function with the smooth transition function $T_w : \mathbb{R} \rightarrow (0, 1)$.
- (b) Relabeling and reinterpreting $f_O(\mathbf{r})$ and $f_B(\mathbf{r})$ as upper and lower contrast bounds, C_H and C_L . In the simplest case where there is a single object in the field, these are constant. For the problems of interest in

instead of CSRBFs and forgo compactness in favor of retaining a norm, rather than a pseudo-norm. This choice facilitates the comparative analysis of the expressiveness and numerical properties of the proposed approach over the so-called RBF PaLS. However, we note that the parameterization we develop in this paper, as well as the analysis, can be utilized in a CSRBF framework as well.

this paper, both C_L and C_H are functions of space whose structures are discussed in section 3.1.

2. **Shape-expressiveness** is expanded by replacing the scalar dilation coefficient, β_j by a matrix \mathbf{R}_j implementing what we are calling stretching and sliding. For 2D problems, each \mathbf{R}_j depends on one element of β and one of γ for a total of 2 parameters per basis function. In the 3D case, this changes to three β 's and three γ 's per \mathbf{R}_j , for a total of 6 parameters per basis function.
3. **Numerical performance** is improved by
 - (a) Fixing the basis function centers on a grid of pre-specified points, χ_j so that these quantities are no longer estimated as part of the inversion process, and combined with the new parameterization, reducing the dimension of the search space with fewer number of parameters.
 - (b) Constraining the size of the expansion coefficients using a $\sigma_h(\alpha_i) \in (-1, 1)$ defined in (3.10).
 - (c) Replacing RBFs, that have non-unique mapping of parameters to c-level sets, with the new ABFs.

In the remainder of this section we discuss the manner in which the model addresses each of these three issues in turn. For the sake of visualization, we focus on the 2D case; however, the ideas carry over to 3D which will be explored in section 4.4.

3.1. Multi-contrast, Single Level Set Reconstructions. In the previous section, we assumed that the property function $f(\mathbf{r})$ had a binary structure, i.e., each point in Ω either belongs to the region O or the background. However, it may well be the case that we have to represent regions containing objects with more than two contrast values [4, 30, 50, 65, 76]. To solve this problem, we replace the Heaviside function in the original PaLS model with a transition function $T_w(x)$ which smoothly, and monotonically varies from zero and one. Specifically, in this paper we take

$$(3.3) \quad T_w(x) = \frac{1}{2} \left[1 + \frac{2}{\pi} \tan^{-1} \left(\frac{\pi x}{w} \right) \right]$$

where w determines the steepness of the transition region. The approximate Heaviside function used in the original PaLS work also monotonically increased from zero to one [2] and thus is similar to T_w . The difference lies in the width of the transition. As seen in Figure 3.1a, for the approximate Heaviside, the transition region is by construction very narrow as the goal was to represent binary valued objects whose “phases” are separated by a narrow diffuse interface. In the new formulation, we increase w to stretch the width of this transition region so that, from (3.1), $f(\mathbf{r})$ can assume basically *any* value between C_L and C_H as seen in Figure 3.1b.

An illustration. To illustrate the impact of these changes to the PaLS model, in Figure 3.2a we display an image of size 82×82 pixels comprised of four piecewise constant objects on a zero-contrast background along with our PaLEnTIR reconstruction in Figure 3.2b. In this case we took the forward model to be the identity so that $\mathbf{d} = \mathbf{f}(\mathbf{p}) + \mathbf{w}$ where $\mathbf{f}(\mathbf{p})$, a discrete representation of $f(\mathbf{r}; \mathbf{p}, C_H, C_L)$, is a vector of length $N_{pts} = 82^2 = 6724$ obtained using the discretization process described in section 4 and for ease of notation, we suppress the dependency of f on C_L and C_H . The vector \mathbf{w} contains independent identically distributed Gaussian random variables with variance such that the signal to noise ratio (SNR) is 40 dB. Thus, the estimate of \mathbf{p} was chosen to minimize $\|\mathbf{d} - \mathbf{f}(\mathbf{p})\|_2^2$. We used 121 basis functions centered on an equally spaced 11×11 grid. We chose the upper and lower contrast coefficients, C_H and C_L , as 4 and 0 respectively since the maximum contrast in the image is equal to 4

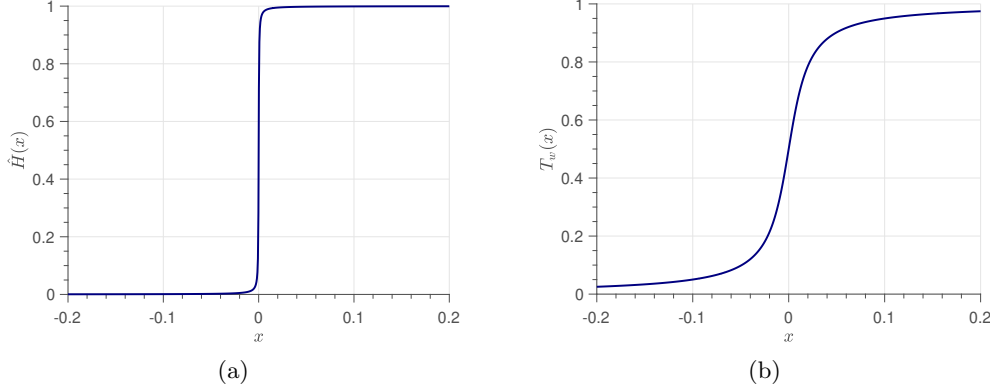


Fig. 3.1: (a) The plot of approximate Heaviside function $\hat{H}(x)$. (b) The plot of the new transition function T_w .

and minimum is equal to 0 which belongs to the background. The TREGS algorithm [66], a regularized trust-region based approach, is used as the optimization method to solve for \mathbf{p} with details are provided in the Appendix.

The mesh plot in Figure 3.2c displays $\phi(\hat{\mathbf{p}})$; that is, the input to $T_w(\cdot)$, which yields the PaLEnTIR reconstructed image in Figure 3.2b. We see that the bright yellow region, whose contrast is equal to C_H , is recovered most accurately. The basis function series in this case takes on relatively large values which are truncated by T_w . The regions where there is no object also look very rough in the mesh plot; however in those areas the basis function series is negative so that the transition function T_w creates a constant, zero-background. Looking at both $\mathbf{f}(\hat{\mathbf{p}})$ as well as the 1D plots of the cuts through the rows 16 and 62 of the recovered images in Figures 3.2d and 3.2e we see mixed results. Both the edges and the contrast of the outer ring in the lower right square annular object with contrast close to the maximum of 4 are accurately recovered. For the remainder of the structures whose contrasts are between 0 and 4, we see blurred edges and oscillations in the contrast that are not dissimilar from what we would expect from least squares denoising.

The strong results in Figure 3.2b in the case of the background and the object in the lower right corner arise from the ability of the transition function to truncate the values of ϕ which are not between C_H and C_L . More generally, PaLEnTIR can achieve similar results across the entire scene by setting C_H and C_L in a space varying manner. The key issue here of course is to do this in a way which retains the advantages of a PaLS-type of model; namely low order and no need for explicit regularization. To motivate our adaptive approach for setting these parameters discussed in Algorithm 3.1, in Figure 3.3 we display a series of three reconstructions for the same problem as in Figure 3.2 where we update the contrast limits iteratively by hand, according to the previous results. To start, we use the “prior knowledge” provided by the results in Fig. 3.2b to manually adjust the elements in the length N_{pts} vector \mathbf{C}_H , our discrete approximations to $C_H(\mathbf{r})$, to those in Figure 3.3b, keeping the corresponding vector \mathbf{C}_L identically equal to zero. The resulting PaLEnTIR reconstruction obtained by using these values of \mathbf{C}_H and \mathbf{C}_L to estimate \mathbf{p} is shown in Figure 3.3c and recovers the blue square and green ovoid with the same fidelity as the yellow annulus from

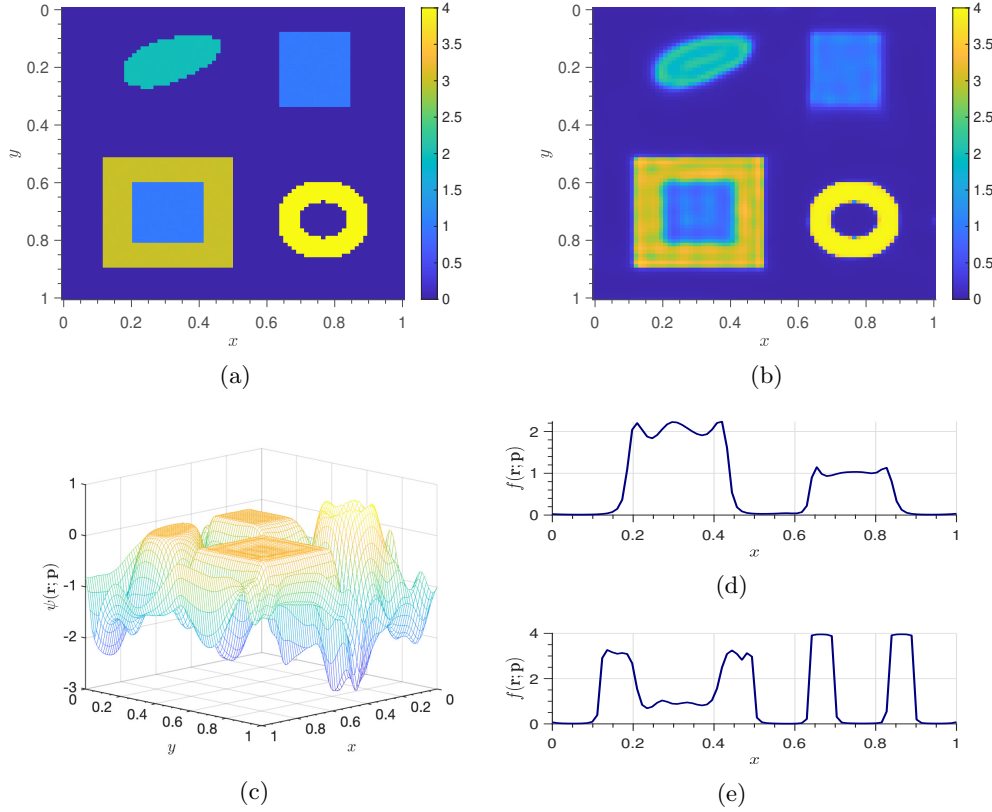


Fig. 3.2: (a) Image comprised of four piecewise constant objects with different shapes and contrasts on a zero-contrast background. (b) The PaLEnTIR reconstruction of the image. (c) Mesh plot and (d,e) cuts of recovered objects through rows 16 and 62 are shown to illustrate the behavior of the basis functions in the new formulation with the transition function.

before. For the reconstructions in the second and third rows of the figure, we update first the \mathbf{C}_H in the second reconstruction in Figure 3.3e and then the \mathbf{C}_L in Figure 3.3g according to the gathered information from the first reconstruction about the location and the contrasts of the nested objects and obtain similar results for the square annulus. The PSNR values of the three PaLEnTIR images are respectively 31.66 dB, 34.45 dB and 37.20 dB.

Algorithm to estimate contrasts. The results in Figure 3.3 and the associated discussion illustrate the ability of the PaLEnTIR model to recover piecewise constant scenes comprised of objects with more than two contrasts using a single level-set function. This feature and its practical utility rest heavily on the ability to specify space-varying bounds on the contrasts at relatively coarse scales. Indeed the need to recover anything approaching “pixelated” versions of these function would nullify any advantages of a PaLS-type approach to inversion. To this end, we write $C_H(\mathbf{r}) = \sum_{n=1}^{N_{pts}} [\mathbf{C}_H]_n \zeta_j(\mathbf{r})$, $C_L(\mathbf{r}) = \sum_{n=1}^N [\mathbf{C}_H]_n \zeta_j(\mathbf{r})$, where $\{\zeta_j\}_{j=1}^{N_{pts}}$ are a set of interpolating basis functions defined using a set of interpolating points $\{\mathbf{r}\}_{n=1}^{N_{pts}}$, $\mathbf{C}_H, \mathbf{C}_L \in \mathbb{R}^{N_{pts}}$

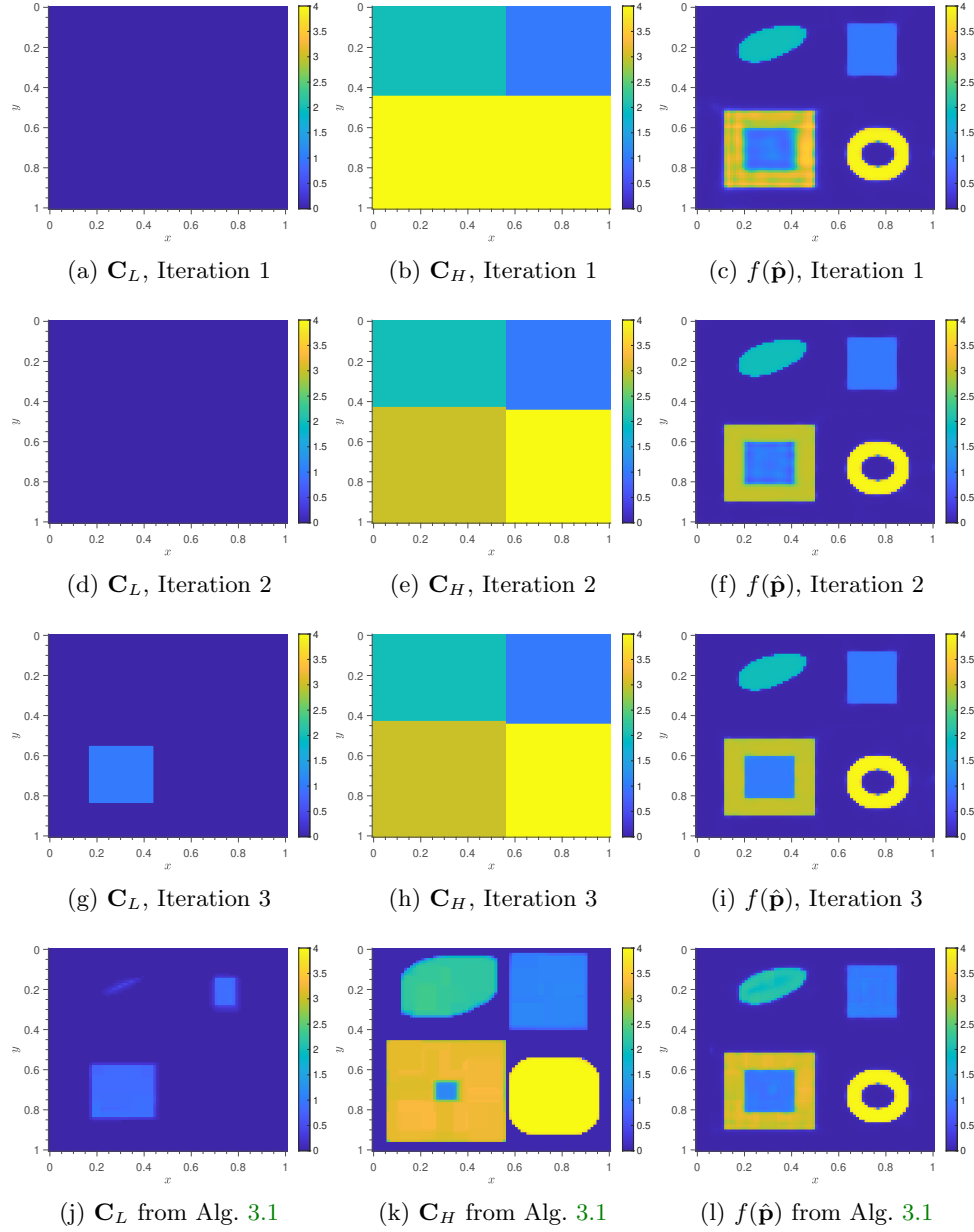


Fig. 3.3: PaLEnTIR Reconstructions of the same objects in Figure 3.2a. (a) - (i) Starting with the reconstruction in Figure 3.2b, $\mathbf{C}_L(\mathbf{r})$ and $\mathbf{C}_H(\mathbf{r})$ are manually updated over three iterations as described in the text. (j)-(l) PaLEnTIR reconstruction using Algorithm 3.1.

are the vectors defining the coefficients in the expansion. Note that, for simplicity, we take the interpolating points $\{\mathbf{r}\}_{n=1}^{N_{pts}}$ to be the same as the pixel locations, but this is not a limitation of our approach and other choices are certainly possible. Here

we propose an iterative algorithm, shown in Algorithm 3.1, to automatically set each \mathbf{C}_L and \mathbf{C}_H , using the `updateC` function defined in Algorithm 3.2, in a deterministic way without abandoning the advantages of PaLS. We begin by initializing the \mathbf{C}_H and \mathbf{C}_L as constants. The best performance is achieved when they are initialized to the maximum and minimum contrast values of the desired image uniformly. We have found that the ultimate performance is not sensitive to the precise choices here. In each iteration, we start by solving a non-linear least squares problem using the current values for \mathbf{C}_H and \mathbf{C}_L . An estimate of the image is then obtained as $f(\hat{\mathbf{p}}^{(k)})$. Using the solution of the non-linear least squares problem, $[\mathbf{C}_H]_n$ (resp. $[\mathbf{C}_L]_n$) is updated to the maximum (resp. minimum) value of $f(\hat{\mathbf{p}}^{(k)})$ within a square window centered at the n^{th} pixel and side length of δ pixels. If the relative change to the previous value of either $[\mathbf{C}_H]_n$ or $[\mathbf{C}_L]_n$ for a given n is less than a threshold then the algorithm skips the update. This rule is not mandatory and if it is removed, we have observed that the algorithm still converges. The reason for us to use this rule is rather practical, we observed that the algorithm converges much faster and to a better objective score. The algorithm converges and stops when relative decrease in the residual norm drops below a small threshold, ρ in Algorithm 3.1, or the square of residual norm drops below the error tolerance, φ in Algorithm 3.1, or maximum number of iterations is reached.

Algorithm 3.1 The main algorithm of PaLEnTIR

Require: $\mathbf{p}_{\text{initial}}, \mathbf{C}_{\min}, \mathbf{C}_{\max}, \mathbf{d}, \rho, \varphi, N_{pts}, \eta, \delta, k_{\max}$

```

1:  $\mathbf{F}^{(-2)} = +\infty$ 
2:  $\mathbf{C}_H^{(-1)} = \mathbf{C}_{\min}$  and  $\mathbf{C}_L^{(-1)} = \mathbf{C}_{\max}$ 
3:  $\hat{\mathbf{p}}^{(-1)} \in \arg \min_{\mathbf{p} \in \mathbb{R}^{n_p}} \frac{1}{2} \|\mathcal{M}(\mathbf{f}(\mathbf{p})) - \mathbf{d}\|_2^2$ 
4:  $\mathbf{F}^{(-1)} = \mathcal{M}(f(\hat{\mathbf{p}}^{(-1)})) - \mathbf{d}$ 
5:  $k = -1$ 
6: while  $\frac{\|\mathbf{F}^{(k-1)} - \mathbf{F}^{(k)}\|_2^2}{\|\mathbf{F}^{(k-1)}\|_2^2} \geq \rho$  or  $\|\mathbf{F}^{(k)}\|_2^2 > \varphi$  or  $k \leq k_{\max}$  do       $\triangleright \rho$ : threshold,
7:    $k = k + 1$                                            $\triangleright \varphi$ : error tolerance
8:    $\mathbf{C}_H^{(k)} = \text{updateC}(\mathbf{f}(\hat{\mathbf{p}}^{(k-1)}), \mathbf{C}_H^{(k-1)}, N_{pts}, \eta, \delta, \text{max})$ 
9:    $\mathbf{C}_L^{(k)} = \text{updateC}(\mathbf{f}(\hat{\mathbf{p}}^{(k-1)}), \mathbf{C}_L^{(k-1)}, N_{pts}, \eta, \delta, \text{min})$ 
10:   $\hat{\mathbf{p}}^{(k)} \in \arg \min_{\mathbf{p} \in \mathbb{R}^{n_p}} \frac{1}{2} \|\mathcal{M}(\mathbf{f}(\mathbf{p})) - \mathbf{d}\|_2^2$ 
11:   $\mathbf{F}^{(k)} = \mathcal{M}(\mathbf{f}(\hat{\mathbf{p}}^{(k)})) - \mathbf{d}$ 
12: end while
Ensure:  $\hat{\mathbf{p}}^{(k)}, \mathbf{C}_H^{(k)}, \mathbf{C}_L^{(k)}$ 

```

Algorithm 3.2 `updateC`

Require: $\mathbf{f}, \mathbf{C}_{\text{prev}}, N_{pts}, \eta, \delta, \text{minORmax}$

```

1:  $\mathbf{C} = \mathbf{C}_{\text{prev}}$                                            $\triangleright$  Initialize  $\mathbf{C}$ 
2: for  $n = 1 : N_{pts}$  do
    $C_{\text{temp}} = \min_{m \in W_{\delta,n}} \text{ORmax} \mathbf{f}_m$        $\triangleright W_{\delta,n}$ : Window of size  $\delta$  centered at  $n$ -th pixel
3:   if  $\left| 1 - \frac{C_{\text{temp}}}{[\mathbf{C}_{\text{prev}}]_n} \right| > \eta$  then           $\triangleright$  Skip if the relative change is below  $\eta$ 
4:      $[\mathbf{C}]_n = C_{\text{temp}}$ 
5:   end if
6: end for
Ensure:  $\mathbf{C}$ 

```

Figure 3.3 (j)-(l) shows the reconstructed image using the method as well as the final contrast coefficients. We started the first reconstruction with uniform contrast coefficients, $\mathbf{C}_H = 4\mathbf{e}$ and $\mathbf{C}_L = 0\mathbf{e}$, where $\mathbf{e} \in \mathbb{R}^{N_{pts}}$ is a vector of ones. The \mathbf{C}_H and \mathbf{C}_L parameters converged after the third iteration to those in Figures 3.3j and 3.3k. The PSNR of the reconstructed image improved significantly compared to the previous reconstruction in Figure 3.2, from 28.71 dB to 34.93 dB to be compared with the PSNR of 37.20 dB in Figure 3.3i which was obtained assuming the bounds were known *a priori*.

3.2. Advancements in the shape-expressiveness. Radial basis functions (RBFs) provide flexibility in representing a large class of shapes and they are very commonly used in PaLS methods. The RBF PaLS is capable of reconstructing the shapes with a very small number of terms in a PaLS representation. However, there are some drawbacks of this formulation. One of the issues is that RBFs can only produce circular cross-sections. For certain classes of shapes, such as those that are highly anisotropic, the use of circular cross sections is inefficient [24]. It is also stated in [24] that 3D models using the RBF representation, as in [44], are limited in their expressiveness due to the spherical effects in the reconstructed objects. For more detail, the comparison of the RBFs and ellipsoidal basis function representations for a 3D problem can be found in [24]. Motivated by these observations, we replace the RBFs in the old PaLS [2] with a model of the form

$$(3.4) \quad \psi(\mathbf{r}) = e^{-\|(\mathbf{R}(\mathbf{r}-\mathbf{x}))\|_2^2},$$

where \mathbf{R} will be a 2×2 matrix for 2D problems and 3×3 for 3D problems. As in [24], this model produces elliptical cross sections however the parameterization of \mathbf{R} is new. We discuss the 2D and 3D cases separately.

2D Stretch and Slide Matrix. In the 2D case we define

$$(3.5) \quad \mathbf{R} = \mu \begin{bmatrix} e^\beta & \gamma \\ 0 & e^{-\beta} \end{bmatrix}$$

where as will be shown below, β and γ define the eccentricity and orientation of the elliptical level sets while μ impacts the scale of the ellipses. In this paper, β and γ are parameters to be determined while we consider μ to be fixed which we explain below.

To understand this model in a bit more detail, we consider the geometry of its level sets for $N = 1$ case, comparing them to those generated from the original PaLS approach. We first define the c -level set representation of a curve Γ as $\Gamma = H(\phi(\mathbf{r}, \mathbf{p}) - c)$; that is, Γ is formed from the set of points \mathbf{r} such that $\phi(\mathbf{r}, \mathbf{p}) = c$ where we take $c > 0$. In the 2D case we have

$$(3.6) \quad \Gamma = \{(x, y) \in \mathbb{R}^2 | \phi(x, y, \mathbf{p}) = c\}.$$

We begin by examining the PaLS c -level set of a single RBF centered at the origin:

$$(3.7) \quad \phi_{\text{rbf}}(x, y, \alpha, \beta) = \alpha e^{-\beta(x^2+y^2)}.$$

Using ϕ_{rbf} in (3.6) and noting that, with $c > 0$ we require $\alpha > 0$ as well to obtain a nonempty shape, simple algebra gives

$$(3.8) \quad \Gamma_{\text{rbf}} = \left\{ (x, y) \in \mathbb{R}^2 \left| x^2 + y^2 = \frac{1}{\beta} \ln \frac{\alpha}{c} \right. \right\}.$$

Eq. (3.8) defines a circle with radius $\sqrt{\frac{1}{\beta} \ln \frac{\alpha}{c}}$. As anticipated, the PaLS c -level set using a single RBF can only produce a circular cross section with a radius defined by the parameters α, β , and c in the manner indicated in (3.8). We emphasize there that with c fixed, there are an infinite number of (α, β) pairs that will give the same circle.

Next, we consider the c -level set for the new model with $N = 1$ where ϕ is

$$(3.9) \quad \phi(x, y, \alpha, \mathbf{R}) = \sigma_h(\alpha) e^{-([x \ y] \mathbf{R}^T \mathbf{R} [x \ y]^T)}.$$

The function $\sigma_h(\cdot)$ is taken in this paper as

$$(3.10) \quad \sigma_h(\alpha) = \tanh\left(\frac{\alpha}{2}\right) = \frac{1 - e^{-\alpha}}{1 + e^{-\alpha}}.$$

Notice that $\sigma_h(\cdot)$ is used to bound the weight coefficient of the basis function between -1 and 1 . Using ϕ in (3.6), again for (α, β, γ) pairs that produce a non-empty set for Γ , which requires $\alpha > 0$ since $c > 0$, if we divide both sides by $\sigma_h(\alpha)$ and take the logarithm of both sides we get

$$(3.11) \quad \Gamma_{\text{new}} = \left\{ (x, y) \in \mathbb{R}^2 \left| e^{2\beta} x^2 + (2\gamma e^\beta) xy + (\gamma^2 + e^{-2\beta}) y^2 = \frac{1}{\mu^2} \ln \frac{\sigma_h(\alpha)}{c} \right. \right\}.$$

When β and γ are 0, similar to Γ_{rbf} , Γ_{new} becomes a circle with a radius of τ where $\tau^2 = \frac{1}{\mu^2} \ln \frac{\sigma_h(\alpha)}{c}$. The function $\sigma_h(\cdot)$ effectively bounds the radius of the c -level set to lie between 0 and $\frac{1}{\mu^2} \ln \frac{1}{c}$. As we discuss in greater depth in section 3.3, this constraint on the size of the expansion coefficient in ϕ is critical to improving the numerical performance of our method as seen in the conditioning of the Jacobian matrix. This analysis also indicates that μ and c basically serve to define the largest possible circle representable using PaLEnTIR. While there may well be use in estimating one or both of these quantities along with the other model parameters, here we choose to set them as constants. Specifically c is set to 0.01, a value slightly larger than 0, due the reasons discussed in [2] and μ is set to 10 to have the maximum area of single ABF to be slightly less than 15% of the total area to restrict the ABFs overlapping each other.

When β and γ are nonzero, the Γ_{new} curve becomes elliptical. To understand the role of each parameter in defining the geometry of the ellipse we start by viewing \mathbf{R} as the Cholesky factor of the symmetric positive definite (SPD) matrix $\mathbf{A} = \mathbf{R}^T \mathbf{R}$ which we call the *Stretch and Slide Matrix*. This matrix includes two types of parameters which are estimated by the PaLEnTIR reconstruction: the *stretching* parameter β and the *sliding* parameter γ . In Figure 3.4a, the impact of the *stretching* parameter β is shown. With $\gamma = 0$, nonzero values of β produce ellipses with principle axes in the cardinal directions. We visualize the impact of increasing β as someone holding the the circle (assuming $\beta = 0$ initially) at two opposing points touching either of the cardinal axes (points shown with green dots in Figure 3.4a), and stretching in the direction of green dashed arrows shown in Figure 3.4a. We call this shape transformation “stretching,” and hence β as the *stretching* parameter. Similarly, as shown in Figure 3.4b γ is the *sliding* parameter because increasing γ horizontally “slides” the maximum and the minimum points of the ellipse on the vertical axes as shown in with red dashed arrows. Due to the fact that the determinant of \mathbf{A} is 1, these two shape transformations do not change the area of the ellipse. The area depends on the constants μ , c , and the parameter α . In summary, with c and μ fixed, α controls the total area by homogeneously expanding the shape, β controls the upper and lower

tangent lines by stretching the ellipse, and γ slides the tangent points of the ellipse over the tangent lines.

If we compare (3.8) and (3.11), we can clearly see that β of ϕ_{rbf} , which adjusts the scale of the circles, is replaced with μ^2 . As we explained above, parameters α and β in ϕ_{rbf} do have the same effect on the c -level set and there are infinite (α, β) pairs for ϕ_{rbf} that will give us the exact same Γ_{rbf} . Hence we replaced β of ϕ_{rbf} with a fixed constant μ^2 to reduce the dimension of the search space of the model and use only the parameter α to determine the scale of the ellipses.

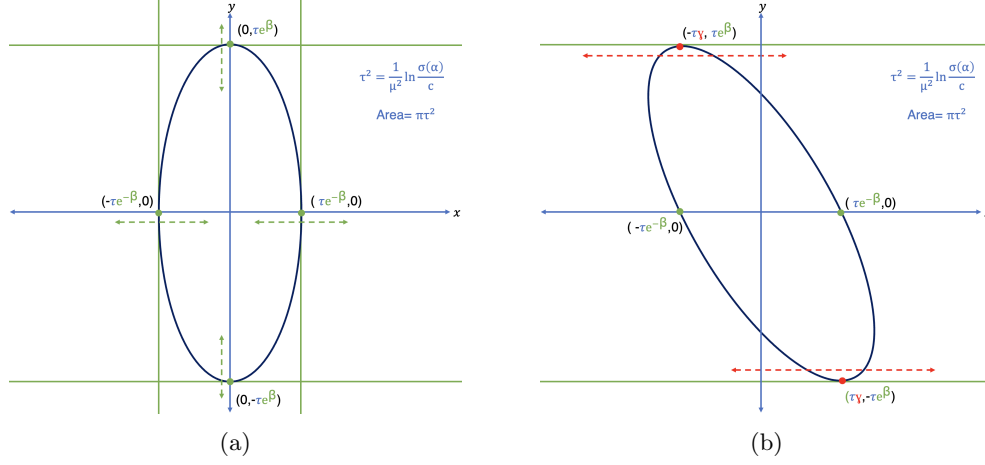


Fig. 3.4: The impact of the parameters on the c -level ellipsoidal representation of the new basis function. (a) shows the impact of the *stretching* parameter β and (b) shows the impact of the *sliding* parameter γ .

3D Dilation Matrix. For the 3D case, we construct $\mathbf{R}_3 \in \mathbb{R}^{3 \times 3}$ using three stretch and slide matrices as follows

$$(3.12) \quad \mathbf{R}_3 = \mu \begin{bmatrix} e^{\beta_1} & \gamma_1 & 0 \\ 0 & e^{-\beta_1} & 0 \\ 0 & 0 & 1 \end{bmatrix} \times \begin{bmatrix} 1 & 0 & 0 \\ 0 & e^{\beta_2} & \gamma_2 \\ 0 & 0 & e^{-\beta_2} \end{bmatrix} \times \begin{bmatrix} e^{\beta_3} & 0 & \gamma_3 \\ 0 & 1 & 0 \\ 0 & 0 & e^{-\beta_3} \end{bmatrix}.$$

Note there are six parameters in our model with each of the three matrices in the product affecting a shear transformation in a 2D plane within \mathbb{R}^3 . Similar to 2D case, \mathbf{R}_3 creates anisotropy in x, y, z and, assuming all three β_i are finite, may be viewed as a Cholesky factor for a 3×3 symmetric positive definite (SPD) matrix $\mathbf{A} = \mathbf{R}_3^T \mathbf{R}_3$. We note that in the 3D PaLS model in [24], the authors do modify the CSRBF formulation to use a matrix-based dilation in order to define ellipsoids. Unlike what we propose here their method uses a symmetric 3×3 parameterized by the six unique elements of such a structure. One of the advantages of our formulation is that $\mathbf{R}_3^T \mathbf{R}_3$ is always SPD whereas, in the 3D PaLS model in [24], regularization is required to enforce this constraint.

3.3. Numerical improvements and stability. Relative to RBF PaLS, the numerical performance of PaLeNTIR is improved as a results of three aspects of the model: the reduction in the number of parameters by fixing the centers of ABFs,

the use of the tanh function to bound the weight parameters modifying the basis functions, and uniqueness of parametric representation of shapes by replacing RBFs.

Here we use the condition number of the Jacobian matrix as the basis for quantifying numerical performance. Recall that the condition number measures the sensitivity to perturbations of the solution to a linear system of equations. As discussed in [20, 31, 70], this is a key metric in determining the performance of a Newton-type approach to estimation of the model parameters. We defined the condition number of the Jacobian as the ratio of the largest to smallest singular value. Values of condition number near 1 indicate a well-conditioned matrix, and large values indicate an ill-conditioned matrix.

For the original PaLS model, as we demonstrate below, the conditioning of the Jacobian worsens as the weight parameters α_i grow in magnitude. By using the hyperbolic tangent function $\sigma_h(\cdot)$ shown in (3.10), the weights of the basis function are bounded between ± 1 , hence it is not possible for a basis function to take on large positive and negative values which would produce poorly conditioned Jacobian matrices. To demonstrate this effect, we empirically explore how the uniqueness of parametric representation of shapes impacts the conditioning of the Jacobian matrix on a simple toy problem. To begin we recall from section 3.2 that the mapping of PaLS parameters to c -level sets is non-unique. We could produce the same circle from the RBF cross section with many parameter sets. This non-uniqueness directly impacts the conditioning of the Jacobian.

To illustrate, we compare the Jacobian conditioning of the RBF PaLS formulation and PaLEnTIR with the new ABFs for the single basis function case. Since RBFs are only capable of producing circular cross sections as discussed in section 3.2, we compare each model’s conditioning when the both basis functions form the same circle with their c -level set representation.

Figure 3.5 shows the base 10 logarithm of the condition numbers of the Jacobian matrices of both models as α is varied with each panel corresponding to a circle of a given radius. The image domain in $[-1, 1]^2$, hence a diameter of 0.4 corresponds to 20% of the total width of the image. In the case of PaLEnTIR, there is a unique parameter set for the proposed ABF to produce a circular cross section with a specific radius since for a circular cross section β and γ must be 0 and radius of the circle $r^2 = \frac{1}{\mu^2} \ln \frac{\sigma_h(\alpha)}{c}$. Hence, there is only a single condition number for PaLEnTIR in each plot, and it is drawn with a red straight line. In the case of RBF PaLS, there are infinitely many parameter pairs of α and β since $r^2 = \frac{1}{\beta} \ln \frac{\alpha}{c}$. For this reason the horizontal axes of plots in the figure correspond to α values with which the RBF produced the desired circular cross section. The β values for the RBF are not shown since it can be calculated by using (3.8) as $\beta_{\text{rbf}} = r^{-2} \ln \frac{\alpha}{c}$. The condition number of the RBF PaLS is shown with the blue line for α values between 0.1 to 240. Notice for all three examples, the ABF shows better or similar performance in terms of the condition number. Moreover, RBF PaLS shows very poor performance around several α values. In all three cases we see many points corresponding to the “spikes” in Figure 3.5 where RBF PaLS produces Jacobian matrices that may well be singular. For this simple case at least, such behavior is not seen when using PaLEnTIR.

For the numerical comparison in a more realistic scenario, we consider the performance of both PaLEnTIR and RBF PaLS on a denoising problem. The 32×32 true image is provided in the Appendix. We ran 100 reconstructions apiece using both RBF PaLS and PaLEnTIR each with 36 basis functions. In each run, we corrupted the data with 1% additive, white, Gaussian noise. Figure 3.6 plots the average con-

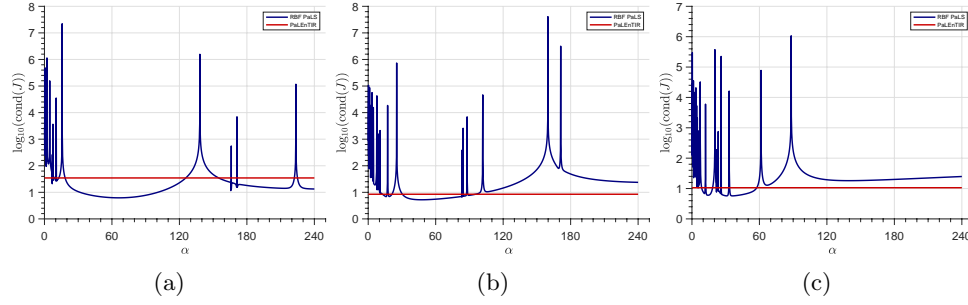


Fig. 3.5: Comparison of Condition number of the Jacobian for RBF PaLS and PaLeNTIR over α values of the RBF PaLS. Each figure compare the model's conditioning when the both models produce the same circle with their c -level representation. The experiment is repeated for producing 3 circles with different radii. (a) shows the plots for producing circle with the radius of 0.1, (b) with 0.16 and (c) with 0.2. The red line represents the PaLeNTIR, and the blue line represents the RBF PaLS.

ditioning of the Jacobian and the convergence when using both PaLeNTIR and RBF PaLS. The convergence score is calculated as $\|\mathbf{F}^{(k)}\|_2^2$ where \mathbf{F} is the residual and defined in the Algorithm 3.1. The stopping criteria for each run are the same as in the Algorithm 3.1. Additionally there is a 10000 iteration limit. For the runs in which the iteration limit is not triggered, the last condition number and the residual value are used for padding the remaining iterations in order to have the same size of residual and condition number vectors for averaging. Figure 3.6a illustrates the strength of PaLeNTIR in significantly improving the average conditioning of the Jacobian compared to the RBF PaLS. In Figure 3.6b we observe the average convergence plots of the two models. PaLeNTIR manages to converge to a better residual more quickly.

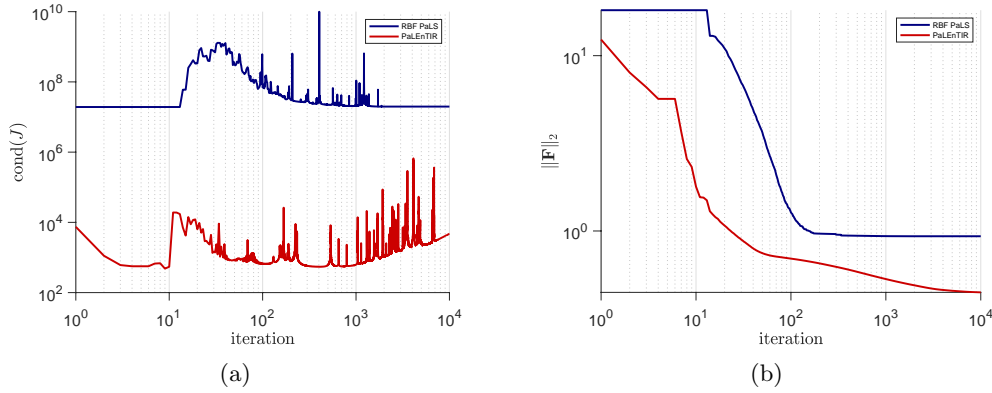


Fig. 3.6: (a) Condition number of the Jacobian matrix and (b) the mismatch score $\|\mathbf{F}^{(k)}\|_2$ plots over TREGS [66] iterations formed by averaging 100 different runs of the optimizer with for each run having a different \mathbf{w} realization. Blue line is for RBF PaLS and red line is for the new PaLeNTIR. Both plots are in Log-log scale.

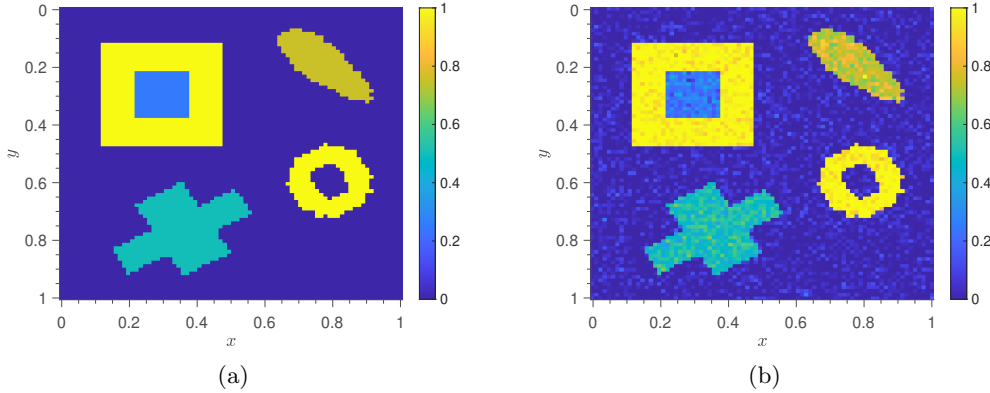


Fig. 4.1: (a) Synthetically generated image of four objects. (b) Input image that is exposed to additive Gaussian noise.

4. Experimental evaluation. We explore the utility of PaLEnTIR using a variety of linear and nonlinear forward models, particularly for problems where the data are limited. All experiments require that we use a discrete form of the forward model developed in section 2. To keep the discussion simple, we will assume that a quadrature rule is used for all integral operators or finite differences if the forward operator involves a PDE. We could use other methods of discretization, but these assumptions permit a straightforward extension of the continuous to discrete notation for purposes of this paper: that is, the vector of unknowns will represent values of the desired function $f(\mathbf{r}; \mathbf{p}, C_H, C_L)$ at a finite set of grid points. Specifically, suppose that $\mathbf{r}_i, i = 1, \dots, N_{pts}$ denotes a discrete set of points in Ω (i.e. each \mathbf{r}_i represents a 2D or 3D spatial grid point). We will define the length- N_{pts} vector $\mathbf{f}(\mathbf{p})$ such that $[\mathbf{f}(\mathbf{p})]_i = f(\mathbf{r}_i; \mathbf{p}, C_H, C_L)$. Suppressing the dependency of f on C_L and C_H for ease of notation, in this discrete case, $\mathcal{M}(\mathbf{f}(\mathbf{p}))$ represents the measured data for all sources given the discrete values $f(\mathbf{r}_i; \mathbf{p})$. The discrete forward model is thus

$$(4.1) \quad \mathbf{d} = \mathcal{M}(\mathbf{f}(\mathbf{p})) + \mathbf{w}.$$

We use Algorithm 3.1 to solve for $\mathbf{f}(\mathbf{p})$.

For each of the problems below, it suffices to indicate the particular forward mapping $\mathcal{M}(\mathbf{f}(\mathbf{p}))$. Details of the parameter selection, initialization process and optimization methods used to solve for $\mathbf{f}(\mathbf{p})$ are provided in the Appendix.

4.1. Denoising. For the denoising problem the forward mapping is defined as $\mathcal{M}(\mathbf{f}(\mathbf{p})) = \mathbf{f}(\mathbf{p})$.

We used the synthetic image shown in Figure 4.1a comprised of four objects with a total of five contrast values (including the background contrast) each having a complex geometry (sharp edges, nested objects, rotated objects, objects having gap inside). We carried out the experiment with four types of randomness: additive Gaussian noise, salt and pepper noise, multiplicative speckle, and using the true object to generate Poisson data. Figure 4.1b shows the resulting data with the Gaussian noise. The image of the data with other types of randomness are provided in the Appendix. The Signal-to-noise ratio (SNR) in decibels of the noisy data are provided in the table in

Figure 4.2. In this paper, SNR is calculated as

$$(4.2) \quad \text{SNR}_{\text{dB}} = 20 \log_{10} \left(\frac{\sqrt{\sum_{n=1}^N |x_n|^2}}{\sqrt{\sum_{n=1}^N |w_n|^2}} \right)$$

where x_n and w_n are the n^{th} element of the noise-free data and the noise respectively.

In the PaLEnTIR model, \mathbf{C}_H and \mathbf{C}_L are initialized as the maximum and minimum values of the whole image and hence $\mathbf{1e}$ and $\mathbf{0e}$ respectively for the experiments whose goal is to reconstruct the image in Figure 4.1a. We use 144 basis functions centered on a 12×12 grid resulting in 432 unknowns. This is over an 85% reduction in parameters compared to the 82×82 array of 6724 pixels comprising the underlying discretization of the image domain.

We compare the performance of the PaLEnTIR model with that obtained using the L2-Total Variation (TV) regularization. For the TV method we used the code in the TVReg Matlab package for Total Variation Reconstruction [37]. For the parameter selection of the L2-TV regularization, we tested over 20000 parameter values for each problem and picked the one with the smallest mean square error thereby providing the best possible result from using this approach. Note that, PaLEnTIR does not require an explicit parameter selection procedure. We compare the both methods according to the following metrics: PSNR (dB), SNR (dB), SSIM, MSE. Structural Similarity Index (SSIM) is a metric that is created to replicate the human visual perception system [77]. The metric compares the two images, the reference image and the one we are interested in, based on three characteristics of an image: luminance, contrast and structure. We use SSIM to reflect visual goodness of an image. A value closer to 1 indicates that the two images are very similar, whereas -1 indicates the opposite. Mean Squared Error (MSE) is a commonly used metric to quantify the difference in the values of each of the corresponding pixels between the sample and the reference images. PSNR is a commonly used metric to quantify the signal quality by comparing the peak level of a desired signal to the level of noise. Both PSNR and MSE are representations of absolute error whereas SSIM gives perception error. Since the experiments showed similar and consistent results, we will mainly focus on the results for the Gaussian noise denoising problem. The performance metrics for the other denoising experiments are also provided in Table 4.1, however the figures and the discussion of these experiments are provided in the Appendix.

4.1.1. Additive Gaussian Noise. Our first experiment is the denoising of an image that is corrupted with the additive Gaussian noise. The input image corrupted with the Gaussian noise is shown in Figure 4.1b. The data SNR of the input is 18.87 dB. The L2-TV and the PaLEnTIR reconstructions of the image are shown in Figure 4.2 and the performance metrics are shown in Table 4.1. Visually, objects in PaLEnTIR reconstruction are much more homogeneous than the ones in the TV reconstruction. For instance, the nested squares on the top left of the image have very rough contrast variations in the TV reconstruction while they are very smooth in PaLEnTIR reconstruction. In both of the reconstructions, there are artifacts in the background. In the TV case there are many small artifacts whereas in PaLEnTIR there are few but larger ones. Since the ROI in this experiment is not the background, this is not a concerning observation. Even using an omniscient approach to selecting the regularization parameter for the L2-TV method, the PaLEnTIR method is superior for all four of the metrics. In terms of absolute error, PaLEnTIR scored better in SNR, PSNR, and MSE metrics. Most notably PaLEnTIR reconstruction achieved

a 0.85 SSIM whereas the L2-TV reconstruction scores only 0.52 as this metric is the most reflective of visual goodness and supports our visual critiques.

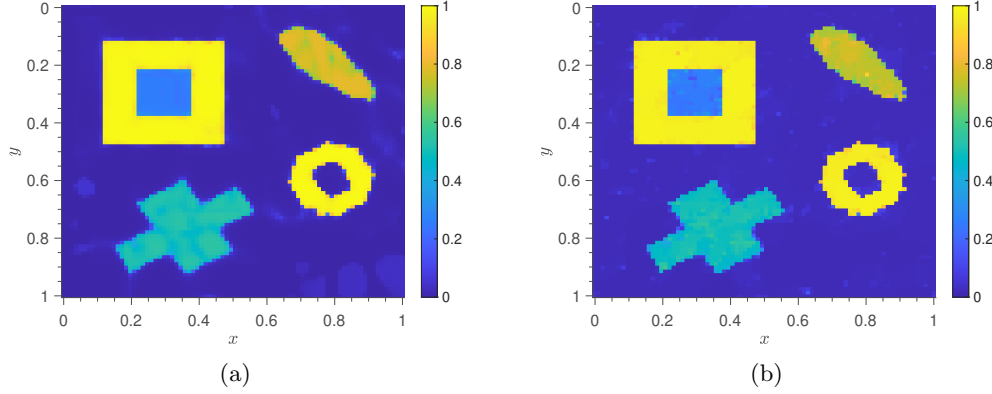


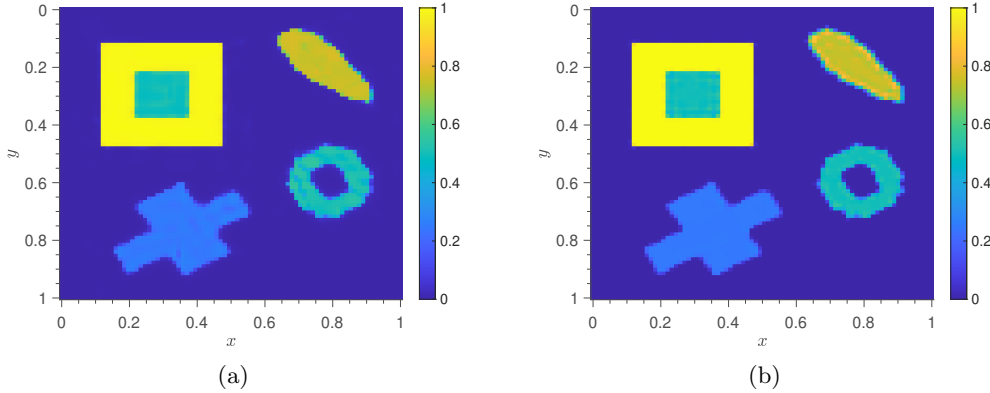
Fig. 4.2: (a) PaLEnTIR reconstruction and (b) L2-TV reconstruction for the Gaussian denoising problem.

Performance Metrics of the Denoising Experiment with Gaussian Noise						
Method	Noise Type (Data SNR)	Unknowns	PSNR	SNR	SSIM	MSE
Total Variation	Gaussian	6724	29.89	22.30	0.52	1e-03
PaLEnTIR	18.87 dB	432	30.99	23.40	0.85	8e-04
Total Variation	Salt&Pepper	6724	24.85	17.26	0.53	3.3e-03
PaLEnTIR	12.99 dB	432	27.44	19.85	0.90	1.8e-03
Total Variation	Poisson	6724	28.34	20.75	0.92	1.5e-03
PaLEnTIR	17.85 dB	432	29.78	22.19	0.95	1.1e-03
Total Variation	Speckle	6724	29.62	22.03	0.95	1.1e-03
PaLEnTIR	19.40 dB	432	29.63	22.04	0.94	1.1e-03

Table 4.1: The performance metrics of PaLEnTIR and TV reconstructions for all four denoising experiments: 1) Additive Gaussian noise, 2) Salt and pepper noise, 3) Poisson noise, 4) Speckle noise. The better scores for each experiment are written with bold letters.

4.2. Deconvolution. Deconvolution is a linear inverse problem where the desired signal is recovered after it is convolved with a filter or a distortion function associated with an instrument or the physics of the problem [36, 60]. The discrete forward model is defined via (3.1) as in (4.1) with the forward mapping $\mathcal{M}(\mathbf{f}(\mathbf{p})) = \mathbf{A}\mathbf{f}(\mathbf{p})$. \mathbf{A} comes from discretizing an integral equation that represents convolution and \mathbf{w} is a vector of zero mean, independent Gaussian random variables.

In our deconvolution experiment, we seek to reconstruct the image in Figure 4.1a from the filtered and noise corrupted input data. The input data is formed by filtering the desired image with a 7×7 Gaussian kernel with a variance of one pixel. The data SNR of the input is 40 dB. Again, We compare the performance of the PaLEnTIR



Performance Metrics of the Deconvolution Experiment with Gaussian Noise					
Method	Unknowns	PSNR	SNR	SSIM	MSE
Total Variation	6724	31.73	23.14	0.98	6.7e-04
PaLEnTIR	432	33.04	24.46	0.97	5e-04

Fig. 4.3: (a) PaLEnTIR reconstruction and (b) L2-TV reconstruction for the deconvolution problem. The table shows the performance metrics for both methods. The better scores are written with bold letters.

model with that obtained using the L2-Total Variation (TV) regularization. Figure 4.3 shows the L2-TV and PaLEnTIR reconstructions as well as the table of performance metrics. Both reconstructions have reconstructed the edges of the shapes quite accurately and each region appears homogeneous except the TV reconstruction of the rotated ellipsoidal shape located at the upper right corner of the image. The TV reconstruction of the ellipsoidal object has noticeably prevalent inhomogeneities, and the boundary of the object is mildly blurred. Both reconstructions have achieved admirable SSIM scores. However, due to visually perfect TV reconstructions of the two objects located in the lower part of the figure, the L2-TV method has a higher SSIM score. In terms of absolute error, again PaLEnTIR outperforms in other three performance metrics.

4.3. X-ray Computed Tomography. X-ray computed tomography (CT) is typically well approximated as a linear problem and is one of the most common and well-known methods for medical imaging applications [17, 38]. As with deconvolution, the forward model takes the form of a matrix vector product, i.e. $\mathcal{M}(\mathbf{f}(\mathbf{p})) = \mathbf{R}\mathbf{f}(\mathbf{p})$ where \mathbf{R} denotes a (discrete) Radon transform, and the vector $\mathcal{M}(\mathbf{f}(\mathbf{p}))$ denotes the vectorized form of the sinogram data. In this paper, we explore the performance of PaLEnTIR on both two and three dimensional forms of the CT problem focusing specifically on cases where there are a limited number of views.

4.3.1. 2D Tomography. For our 2D experiments, we use an open-access data set of tomographic X-ray data of carved cheese [12]. The image of the carved cheese as well as the ground truth reconstruction provided in the dataset is shown in Figure 4.4. We consider both sparse angle and limited angle problems. For the sparse angle case we take 15 projections spanning the full 360° circle whereas for the limited angle problem we use 15 projections spanning the range 1° – 90° . In both experiments our

PaLEnTIR model consists of 144 basis functions. The total number of unknowns for the PaLEnTIR model is 432. We compare the PaLEnTIR reconstructions with both L2-TV reconstructions and Tikhonov reconstructions. The code for the Tikhonov method is given in [12]. For both of these reconstructions, the required number of unknowns is equal to $128 \times 128 = 16384$ which is almost 40 times more than the PaLEnTIR model. Both the Tikhonov and L2-TV methods require their parameters to be selected. Unlike the other experiments, we could not directly select the best parameter for these methods. The reason is that the given ground truth data and the FBP data have a different scale/color bar. The parameter value for the Tikhonov method is given in [12]. For the L2-TV method we picked the parameter that gave the highest quality reconstruction visually.

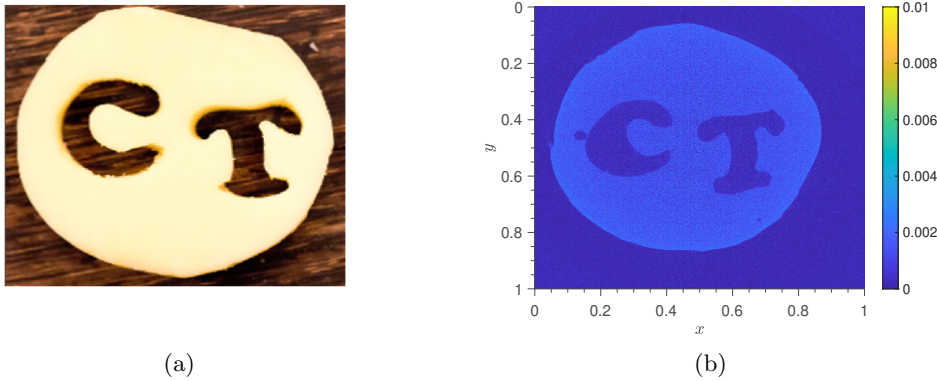


Fig. 4.4: (a) The image of the carved cheese and (b) the ground truth reconstruction of the cheese data provided in dataset [12]. The repository of the data can be found in [13]. The permission for displaying the real image of the carved cheese is granted by the author of the dataset.

4.3.2. Sparse Angle Tomography. The three reconstructions for the sparse-angle problem are shown in Figure 4.5. All three methods are capable of recovering the general shape of the object. The Tikhonov reconstruction suffers from far more artifacts in the background than either L2-TV or PaLEnTIR. Moreover, the small hole to the left of the “C” seen in Figure 4.4a, is recovered poorly in the Tikhonov case. The L2-TV reconstruction is much more successful in recovering the small hole and suppressing the background artifacts. The cheese has a smoother reconstruction in the L2-TV compared to the Tikhonov reconstruction. The PaLEnTIR model with 144 basis functions has also managed to recover the object successfully. The inhomogeneities seen on the cheese surface in Tikhonov and L2-TV methods are less evident in the PaLEnTIR reconstruction. The letters in the PaLEnTIR case look more noisy than the L2-TV approach. However, it is important to note that both the L2-TV and PaLEnTIR reconstructions have background noise. The L2-TV results has more artifacts at a lower contrast whereas PaLEnTIR has fewer artifacts but they are much brighter. Finally, we point out that the small hole near the letter “C” is just as evident in the PaLEnTIR reconstruction as the L2-TV despite the fact that the former employs only about 2.5% of the number of unknowns as the latter.

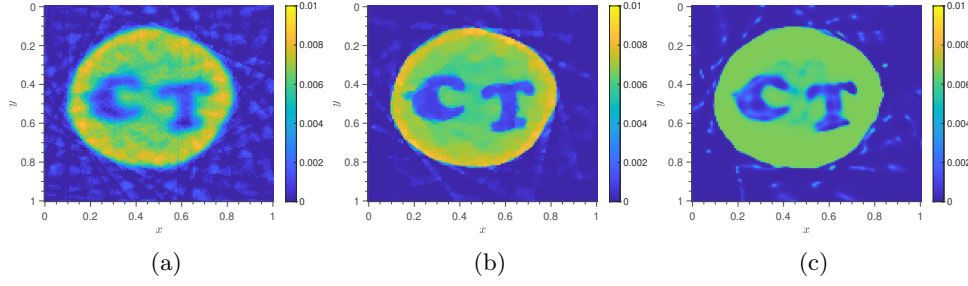


Fig. 4.5: (a) Tikhonov, (b) TV, and (c) PaLEnTIR reconstructions of the sparse angle tomography using the cheese data.

4.3.3. Limited View Tomography. The three limited view reconstructions are shown in Figure 4.4. Here we see far more distortion, especially in the Tikhonov and L2-TV reconstruction than was the case with the sparse angle problem. In the Tikhonov case, it is almost impossible to locate the upper left and lower right parts of the object. The small hole near the letter “C” is completely missing. The L2-TV reconstruction is an improvement in that the upper left and lower right parts are better recovered although the boundary of the object is still blurry. The letters “C” and “T” are clearer compared to the Tikhonov case though they are still blurry. It is still not possible to observe the small hole in the L2-TV. The PaLEnTIR reconstruction eliminates the X-Ray artifacts in most of the image. The upper left and lower right portions (which the L2-TV and Tikhonov struggle to recover) as well as the letters are much clearer. Furthermore, the small hole that is completely lost in the other recoveries is clearly observable in the PaLEnTIR reconstruction. There are far fewer severe artifacts in the PaLEnTIR reconstruction with most located in the background.

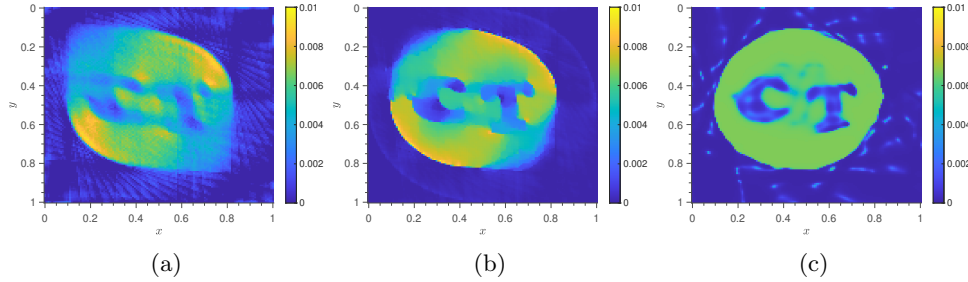
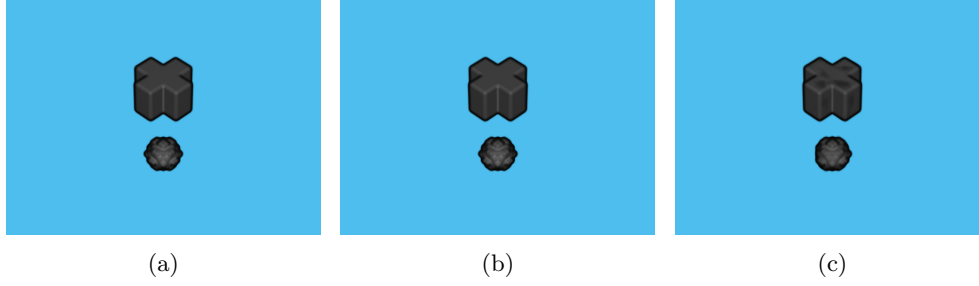


Fig. 4.6: (a) Tikhonov, (b) TV, and (c) PaLEnTIR reconstructions of the limited angle tomography using the cheese data.

4.4. 3D Limited View Parallel Beam Tomography. We now consider a 3D limited view parallel beam tomography experiment. Here, we build the system matrix for the forward mapping in (4.1), using the TVReg Matlab package for Total Variation Reconstruction [37]. The desired 3D image is of size $27 \times 27 \times 27$ shown in Figure 4.7a. The input data is formed from 31 projections where each projection



Performance Metrics of 3D Limited CT					
Method	Unknowns	PSNR	SNR	SSIM	MSE
Total Variation	19683	60.95	48.03	1.00	8e-07
PaLEnTIR	2401	35.17	22.25	0.96	3e-04

Fig. 4.7: Results of 3D limited view parallel beam tomography experiment. (a) original image of the 3D objects, (b) TV and (c) PaLEnTIR reconstructions. The table shows the performance metrics of the PaLEnTIR reconstruction.

has a projection plane center located on the surface of the quarter of a “lebedev sphere” [45] as shown in Figure 4.8. 1% Gaussian noise is added to the input data. We used $7^3 = 343$ basis functions in the PaLEnTIR model. Again, we compare the performance of the PaLEnTIR model with that obtained using L2-Total Variation (TV) regularization. The reconstructed objects are shown in Figure 4.7 along with the performance metrics. TV method beats PaLEnTIR in all four performance metrics. However, PaLEnTIR *employs only about 12% of the number of unknowns as the TV method* and the objects are still well reconstructed with sharp boundaries. With only 343 basis functions, the PaLEnTIR model succeeded in representing a 19683 pixel 3D image with two 3D objects with more than 35 dB PSNR and an SSIM of about 0.96.

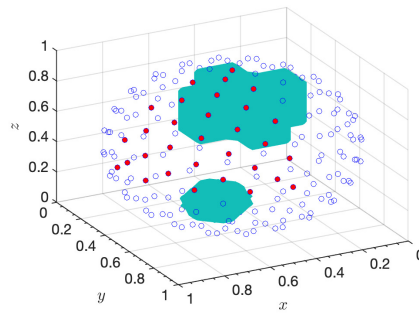


Fig. 4.8: Green objects represent the objects of interest in the 3D CT experiment. Blue points are the samples from a lebedev sphere surrounding the objects and centered at the origin. Red points are the chosen samples from the lebedev sphere to and are used as the projection plane centers in the 3D CT experiment. The projection plane centers are chosen such that they all are located at the same quarter of the sphere.

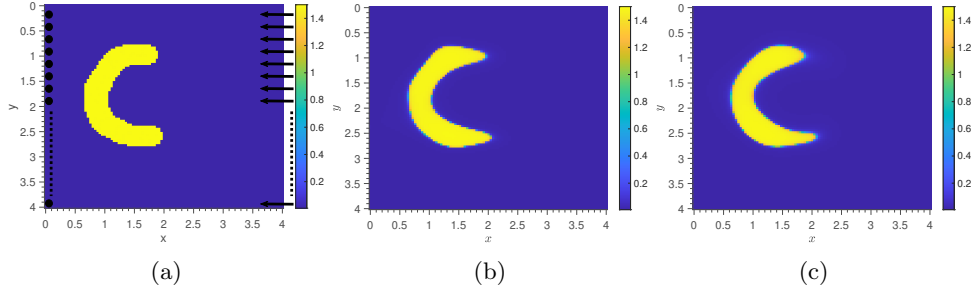


Fig. 4.9: The results of Diffuse Optical Tomography experiment are shown. (a) True anomaly with sources (right) and Detectors (left), (b) reconstruction of the absorption image without additive white noise (SSIM:0.92, MSE:1.46e-2, PSNR:21.87dB, SNR:10.75dB), (c) reconstruction of the absorption image with 1% additive white noise (SSIM:0.89, MSE:1.92e-2, PSNR:20.69dB, SNR:9.57dB).

4.5. Diffuse Optical Tomography. Diffuse optical tomography (DOT) is a non-invasive, low-cost alternative for breast and brain imaging compared with X-ray and MRI [10]. In DOT, the tissue is illuminated with near infra-red light and the data, comprised of point measurements of diffused and partially absorbed photon fields, is collected external to the body. These measurements are used along with a mathematical model, typically a diffusion-absorption equation (posed in the frequency domain), to recover the optical absorption and (sometimes) scattering properties of the medium. Here we use such a model of the form

$$-\nabla \cdot (D(\mathbf{r})\nabla\eta(\mathbf{r})) + \mu(\mathbf{r}; \mathbf{p})\eta(\mathbf{r}) + \frac{i\omega}{\nu}\eta(\mathbf{r}) = g(\mathbf{r}),$$

where $D(\mathbf{r})$ represents (here) the known scalar diffusion at a point \mathbf{r} , $\mu(\mathbf{r}; \mathbf{p})$, the quantity for which we will be inverting, represents the absorption as a function of space and the parameter vector \mathbf{p} , ω represents the modulation frequency of the light source, and ν represents the speed of light in the tissue. The sources are placed one grid point inside the medium [5], and the detectors are placed on the opposite boundary. On the boundaries where the sources and detectors are located we have Robin boundary conditions; on the other boundaries we assume homogeneous Dirichlet boundary conditions, $\eta(\mathbf{r}) = 0$. For details, see [6, 67]. The recovered absorption coefficient (and sometimes also the diffusion/scattering) can then be used to characterize the state of the tissue [10, 27, 28].

Following, e.g., [43], we assume that the absorption coefficient can be modeled via (3.1). As shown in Figure 4.9, we take the region to be imaged as a rectangle of size 4cm by 4cm, with $m_s = 32$ sources arrayed on the right side and $m_d = 32$ detectors on the left. As before, we let $\mathbf{f}(\mathbf{p})$ denote the discrete absorption image for a given parameter vector, that is, $[\mathbf{f}(\mathbf{p})]_i = f(\mathbf{r}_i, \mathbf{p})$ for any grid point \mathbf{r}_i . Assuming we collect data for all detectors when each source is active, we obtain a data vector \mathbf{d} with $m = m_s \times m_d$ values. The input-output map from sources to detectors [61] (also called the *transfer function*) as a function of \mathbf{p} , is given by

$$(4.3) \quad \Psi(\mathbf{f}(\mathbf{p})) = \mathbf{C}^T \mathbf{A}(\mathbf{f}(\mathbf{p}))^{-1} \mathbf{B} \in \mathbb{R}^{m_d \times m_s},$$

where $\mathbf{B} \in \mathbb{R}^{n \times m_s}$ represents m_s sources, n is the total number of voxels or grid

points, $\mathbf{A}(\mathbf{f}(\mathbf{p})) \in \mathbb{R}^{n \times n}$ represents the discretization of the diffusion-absorption equation, and $\mathbf{C}^T \in \mathbb{R}^{m_d \times n}$ simulates the measurement of outputs at m_d detectors. So, $\mathbf{A}(\mathbf{f}(\mathbf{p}))\mathbf{X} = \mathbf{B}$ represents the discretized PDE that relates photon fluence/flux at grid points to the sources [5]. The DOT inverse problem is then specified by the forward mapping $\mathcal{M}(\mathbf{f}(\mathbf{p})) = \text{vec}(\Psi(\mathbf{f}(\mathbf{p})))$, the vectorization of the transfer function output. Given a vector of measured data (with additive noise) \mathbf{d} , we solve for \mathbf{p} by minimizing $\frac{1}{2}\|\text{vec}(\Psi(\mathbf{f}(\mathbf{p}))) - \mathbf{d}\|_2^2$ (cf Algorithm 3.1). Note that regularization is provided implicitly by the parameterization.

We present results for a test case with the true anomaly as shown in Figure 4.9a. The focus of this test is the quality of the shape reconstruction using the new PaLEnTIR parameterization. We note that the DOT problem is severely ill posed, both due to limited numbers of sources and detectors as well as the highly diffuse nature of the problem, so accurate reconstructions are not possible. Indeed, this is why the shape-based parameterized reconstruction for problems with well-defined boundaries is important. To distinguish between reconstruction error due to noise and ill-posedness and reconstruction error due to the nature of the problem, we provide a reconstruction with 1% noise (realistic) as well as one without noise. The latter serves to demonstrate the difficulty of the data limited problem which should be distinguished from the approximation quality of PaLEnTIR.

The reconstruction for the data without noise is shown in Figure 4.9b. The performance metrics are given in the figure description. The model captures the structure quite well with SSIM score of 0.92, with slight imperfections due to the data limited nature of the problem rather than the PaLEnTIR model. When noise is added and we run the algorithm we observe the image in Figure 4.9c and the performance metrics are given in the figure description. While the edges are slightly less clear in the noisy case, the reconstruction is remarkably good with SSIM score of 0.89, given the limitations of the data and the diffusive nature of the forward problem. It is important to note that there was no parameter to tune in generating this reconstruction.

5. Conclusion and Future Work. In this paper, we redefined the parametric level-set method to improve the quality and function of the PaLS approach in solving inverse imaging problems for images with (possibly multiple) piecewise constant contrasts. Our new method, PaLEnTIR, can successfully represent multi-contrast scenes with very few parameters since it is only formulated by a single level-set function in contrast to current state-of-the-art formulations which require multiple level-sets. We thoroughly investigated the qualitative performance of our new model by illustrating that replacing RBFs in PaLS with ABFs expands the family of shapes that can be represented by a single basis function from circles to rotated ellipses. We empirically demonstrated how PaLEnTIR outperformed the RBF PaLS in terms of the condition number of the Jacobian matrix in both single and multiple basis functions cases.

We demonstrated the utility of PaLEnTIR on numerical experiments over a wide range of inverse problems which included 2D and 3D experiments, a test on real data, and tests on both non-linear and linear inverse problems. In the examples where comparisons were made, our reconstructions were at least as good, if not much better, than those computed with competing reconstruction methods whose parameters had been tuned to the optimal values which are not going to be known in practice. The built-in regularization through the parameterization made it possible even in the non-linear, severely data-limited DOT problem, for a high-quality reconstruction. Multiple contrasts in varying shapes and configurations were readily picked up by

our new approach without any hand tuning or regularization parameter selection. In summary, we have demonstrated the power of PaLEnTIR for reconstruction, denoising and restoration for the class of images that are piecewise constant.

The strong performance of PaLEnTIR motivates a number of areas where future efforts are needed. In future work, we will delve more fully into 3D problems and test the model with several different 3D, nonlinear ill-posed problems. While PaLEnTIR worked well using homogeneously distributed basis functions, we believe that the performance of the model can be further improved through the use of some type of adaptive refinement strategy similar to [7, 8] which places more basis functions in regions where there is, in some sense, greater geometric detail. We also will aim for a better understanding the convergence properties of the iteration used to determine C_L and C_H . To supplement the strong numerical results, we believe it should be possible to better understand the behavior of this method at least in the context of simple “toy” problems such as the recovery of a 1D step discontinuity. Finally, we will investigate the use of this model for Uncertainty Quantification focusing on building prior models for the PaLEnTIR parameters from priors on the objects for which we are looking as well as the use of these priors for quantifying e.g., accuracy in localizing and characterizing objects to be recovered.

References.

- [1] R. Acar and C. Vogel. “Analysis of bounded variation penalty methods for ill-posed problems”. In: *Inverse Problems* 10 (1994), pp. 1217–1229.
- [2] Alireza Aghasi, Misha Kilmer, and Eric Miller. “Parametric Level Set Methods for Inverse Problems”. In: *SIAM J. Imaging Sciences* 4 (July 2011). DOI: [10.1137/100800208](https://doi.org/10.1137/100800208).
- [3] Alireza Aghasi et al. “A geometric approach to joint inversion with applications to contaminant source zone characterization”. In: *Inverse problems* 29.11 (2013), p. 115014.
- [4] G. Allaire et al. “Multi-phase structural optimization via a level set method”. In: *ESAIM: Control, Optimisation and Calculus of Variations* 20.2 (2014), pp. 576–611. DOI: [10.1051/cocv/2013076](https://doi.org/10.1051/cocv/2013076).
- [5] S. .R. Arridge. “Optical tomography in medical imaging”. In: *Inverse Problems* Vol. 16 (1999), R41–R93.
- [6] Selin S. Aslan, Eric de Sturler, and Misha E. Kilmer. “Randomized approach to nonlinear inversion combining random and optimized simultaneous sources and detectors”. In: *SIAM J. Sci. Comput* 41 (2019), B229–B249.
- [7] Alexandre Baussard, Eric L Miller, and Dominique Lesselier. “Adaptive multi-scale reconstruction of buried objects”. In: *Inverse Problems* 20.6 (2004), S1.
- [8] Alexandre Baussard, Eric L Miller, and Denis Prémel. “Adaptive B- spline scheme for solving an inverse scattering problem”. In: *Inverse Problems* 20.2 (2004), p. 347.
- [9] M Ben, Mohamed Khames Ben Hadj Miled, and Eric Miller. “A projection-based level-set approach to enhance conductivity anomaly reconstruction in electrical resistance tomography”. In: *Inverse Problems* 23 (Dec. 2007), pp. 2375–2400. DOI: [10.1088/0266-5611/23/6/007](https://doi.org/10.1088/0266-5611/23/6/007).
- [10] DA Boas et al. “Imaging the body with diffuse optical tomography”. In: *IEEE Signal Processing Magazine* 18.6 (2001), pp. 57–75.
- [11] T. Brox and J. Weickert. “Level Set Segmentation With Multiple Regions”. In: *IEEE Transactions on Image Processing* 15.10 (2006), pp. 3213–3218. DOI: [10.1109/TIP.2006.877481](https://doi.org/10.1109/TIP.2006.877481).

- [12] Tatiana A. Bubba et al. *Tomographic X-ray data of carved cheese*. 2017. arXiv: [1705.05732](https://arxiv.org/abs/1705.05732) [physics. med-ph].
- [13] Tatiana A. Bubba et al. *Tomographic X-ray data of carved cheese (1.0.0) [Data set]*. Zenodo. <https://doi.org/10.5281/zenodo.1254210>. Version 1.0.0. May 2017.
- [14] Tony Chan and Luminita Vese. “Active Contours without Edges”. In: *IEEE Transactions on Image Processing* 10 (Jan. 2001), pp. 266–277.
- [15] Chi-Chih Chen et al. “Ultrawide-bandwidth fully-polarimetric ground penetrating radar classification of subsurface unexploded ordnance”. In: *IEEE Transactions on Geoscience and Remote Sensing* 39.6 (2001), pp. 1221–1230.
- [16] W Dailey and A Ramirez. “Electrical impedance tomography of the 1995 OGI perchloroethylene release”. In: (Oct. 1996). DOI: [10.2172/461374](https://doi.org/10.2172/461374). URL: <https://www.osti.gov/biblio/461374>.
- [17] Mark E. Davison. “The Ill-Conditioned Nature of the Limited Angle Tomography Problem”. In: *SIAM Journal on Applied Mathematics* 43.2 (1983), pp. 428–448. DOI: [10.1137/0143028](https://doi.org/10.1137/0143028). eprint: <https://doi.org/10.1137/0143028>. URL: <https://doi.org/10.1137/0143028>.
- [18] Ross W Deming and Anthony J Devaney. “Diffraction tomography for multi - monostatic ground penetrating radar imaging”. In: *Inverse Problems* 13.1 (1997), p. 29.
- [19] Zhiliang Deng, Xiaomei Yang, and Jiangfeng Huang. *A parametric Bayesian level set approach for acoustic source identification using multiple frequency information*. 2019. arXiv: [1907.08660](https://arxiv.org/abs/1907.08660) [math.NA].
- [20] John E Dennis Jr and Robert B Schnabel. *Numerical methods for unconstrained optimization and nonlinear equations*. SIAM, 1996.
- [21] Kees van den Doel and U. Ascher. “On level set regularization for highly ill-posed distributed parameter estimation problems”. In: *Journal of Computational Physics* 216 (Aug. 2006), pp. 707–723. DOI: [10.1016/j.jcp.2006.01.022](https://doi.org/10.1016/j.jcp.2006.01.022).
- [22] Oliver Dorn and Dominique Lesselier. “Level set methods for inverse scattering”. In: *Inverse Problems* 22 (June 2006), R67. DOI: [10.1088/0266-5611/22/4/R01](https://doi.org/10.1088/0266-5611/22/4/R01).
- [23] Oliver Dorn and Dominique Lesselier. “Level set techniques for structural inversion in medical imaging”. In: *Deformable Models*. Springer, 2007, pp. 61–90.
- [24] Moshe Eliasof, Andrei Sharf, and Eran Treister. “Multi-modal 3D Shape Reconstruction Under Calibration Uncertainty using Parametric Level Set Methods”. In: *CoRR* abs/1904.10379 (2019). arXiv: [1904.10379](https://arxiv.org/abs/1904.10379). URL: <http://arxiv.org/abs/1904.10379>.
- [25] H.W. Engl, M. Hanke, and A. Neubauer. *Regularization of Inverse Problems. Mathematics and Its Applications*. Springer Netherlands, 1996. ISBN: 9780792341574. URL: <https://books.google.com/books?id=2bzgmMv5EVcC>.
- [26] Sarah Fakhreddine et al. “Imaging geochemical heterogeneities using inverse reactive transport modeling: An example relevant for characterizing arsenic mobilization and distribution”. In: *Advances in Water Resources* 88 (2016), pp. 186–197.
- [27] Qianqian Fang et al. “Combined optical and X-ray tomosynthesis breast imaging 1”. In: *Radiology* 258.1 (2011), pp. 89–97.
- [28] Qianqian Fang et al. “Combined optical imaging and mammography of the healthy breast: optical contrast derived from breast structure and compression”. In: *Medical Imaging, IEEE Transactions on* 28.1 (2009), pp. 30–42.
- [29] Haihua Feng, William Karl, and David Castanon. “A curve evolution approach to object-based tomographic reconstruction”. In: *IEEE transactions on image*

- processing : a publication of the IEEE Signal Processing Society* 12 (Feb. 2003), pp. 44–57. DOI: [10.1109/TIP.2002.806253](https://doi.org/10.1109/TIP.2002.806253).
- [30] S. J. Hamilton and A. Hauptmann. “Deep D-Bar: Real-Time Electrical Impedance Tomography Imaging With Deep Neural Networks”. In: *IEEE Transactions on Medical Imaging* 37.10 (2018), pp. 2367–2377. DOI: [10.1109/TMI.2018.2828303](https://doi.org/10.1109/TMI.2018.2828303).
 - [31] N.J. Higham. *Accuracy and Stability of Numerical Algorithms: Second Edition*. Other Titles in Applied Mathematics. Society for Industrial and Applied Mathematics, 2002. ISBN: 9780898718027. URL: <https://books.google.com/books?id=7J52J4GrsJkC>.
 - [32] A. J. Hiles and O. Dorn. “Colour level set regularization for the electromagnetic imaging of highly discontinuous parameters in 3D”. In: *Inverse Problems in Science and Engineering* 29.4 (2021), pp. 489–524. DOI: [10.1080/17415977.2020.1797003](https://doi.org/10.1080/17415977.2020.1797003). eprint: <https://doi.org/10.1080/17415977.2020.1797003>. URL: <https://doi.org/10.1080/17415977.2020.1797003>.
 - [33] G. Hoversten et al. “Borehole to Surface Electromagnetic Monitoring of Hydraulic Fractures”. In: June 2017. DOI: [10.3997/2214-4609.201700853](https://doi.org/10.3997/2214-4609.201700853).
 - [34] G. Hoversten et al. “Multi-physics Inversion for Reservoir Monitoring”. In: May 2016. DOI: [10.3997/2214-4609.201601658](https://doi.org/10.3997/2214-4609.201601658).
 - [35] Gabriele Incorvaia and Oliver Dorn. “Stochastic Optimization Methods for Parametric Level Set Reconstructions in 2D through-the-Wall Radar Imaging”. In: *Electronics* 9.12 (2020). ISSN: 2079-9292. DOI: [10.3390/electronics9122055](https://doi.org/10.3390/electronics9122055). URL: <https://www.mdpi.com/2079-9292/9/12/2055>.
 - [36] Peter A. Jansson. “Deconvolution of images and spectra”. In: 1997.
 - [37] Tobias Lindstrøm Jensen et al. *TVReg*. English. 2010.
 - [38] Willi Kalender. “X-ray computed tomography”. In: *Physics in medicine and biology* 51 (Aug. 2006), R29–43. DOI: [10.1088/0031-9155/51/13/R03](https://doi.org/10.1088/0031-9155/51/13/R03).
 - [39] Misha Kilmer et al. “Cortical constraint method for diffuse optical brain imaging”. In: *Advanced Signal Processing Algorithms, Architectures, and Implementations XIV*. Ed. by Franklin T. Luk. Vol. 5559. International Society for Optics and Photonics. SPIE, 2004, pp. 381–391. URL: <https://doi.org/10.1117/12.559745>.
 - [40] Andreas Kirsch. “Characterization of the shape of a scattering obstacle using the spectral data of the far field operator”. In: *Inverse Problems* 14 (1998), pp. 1489–1512.
 - [41] Ville Kolehmainen, Matti Lassas, and Samuli Siltanen. “Limited Data X-Ray Tomography Using Nonlinear Evolution Equations”. In: *SIAM J. Scientific Computing* 30 (Jan. 2008), pp. 1413–1429. DOI: [10.1137/050622791](https://doi.org/10.1137/050622791).
 - [42] R Kress and W Rundell. “A quasi-Newton method in inverse obstacle scattering”. In: *Inverse Problems* 10.5 (Oct. 1994), pp. 1145–1157. DOI: [10.1088/0266-5611/10/5/011](https://doi.org/10.1088/0266-5611/10/5/011). URL: <https://doi.org/10.1088/0266-5611/10/5/011>.
 - [43] Fridrik Larusson, Sergio Fantini, and Eric L Miller. “Parametric level set reconstruction methods for hyperspectral diffuse optical tomography”. In: *Biomedical optics express* 3.5 (2012), pp. 1006–1024.
 - [44] Fridrik Larusson et al. “Parametric estimation of 3D tubular structures for diffuse optical tomography”. In: *Biomedical optics express* 4 (Feb. 2013), pp. 271–86. DOI: [10.1364/BOE.4.000271](https://doi.org/10.1364/BOE.4.000271).
 - [45] Vyacheslav Ivanovich Lebedev. “Quadratures on a sphere”. In: *USSR Computational Mathematics and Mathematical Physics* 16.2 (1976), pp. 10–24.

- [46] R. Li et al. "An Image Reconstruction For Electrical Capacitance Tomography Using Parametric Level Set". In: *2020 5th International Conference on Computer and Communication Systems (ICCCS)*. 2020, pp. 384–390. DOI: [10.1109/ICCCS49078.2020.9118589](https://doi.org/10.1109/ICCCS49078.2020.9118589).
- [47] J. Lie, M. Lysaker, and Xue-Cheng Tai. "A binary level set model and some applications to Mumford-Shah image segmentation". In: *IEEE Transactions on Image Processing* 15.5 (2006), pp. 1171–1181. DOI: [10.1109/TIP.2005.863956](https://doi.org/10.1109/TIP.2005.863956).
- [48] D. Liu, D. Smyl, and J. Du. "Nonstationary Shape Estimation in Electrical Impedance Tomography Using a Parametric Level Set-Based Extended Kalman Filter Approach". In: *IEEE Transactions on Instrumentation and Measurement* 69.5 (2020), pp. 1894–1907. DOI: [10.1109/TIM.2019.2921441](https://doi.org/10.1109/TIM.2019.2921441).
- [49] Dong Liu, Danny Smyl, and Jiangfeng Du. "Comparison of different radial basis functions for parametric level set based method in electrical impedance tomography". In: Sept. 2018.
- [50] Jikai Liu and Yongsheng Ma. "A new multi-material level set topology optimization method with the length scale control capability". In: *Computer Methods in Applied Mechanics and Engineering* 329 (2018), pp. 444–463. ISSN: 0045-7825. DOI: <https://doi.org/10.1016/j.cma.2017.10.011>. URL: <https://www.sciencedirect.com/science/article/pii/S0045782517306795>.
- [51] M.S. McMillan et al. "3D Multiple Body Parametric Inversion of Time-domain Airborne EM Data". In: 2015.1 (2015), pp. 1–5. ISSN: 2214-4609. DOI: <https://doi.org/10.3997/2214-4609.201413870>. URL: <https://www.earthdoc.org/content/papers/10.3997/2214-4609.201413870>.
- [52] Michael Mcmillan et al. "Multiple body parametric inversion of frequency- and time-domain airborne electromagnetics". In: Sept. 2016, pp. 846–851. DOI: [10.1190/segam2016-13868448.1](https://doi.org/10.1190/segam2016-13868448.1).
- [53] F. Mesadi, M. Cetin, and T. Tasdizen. "Disjunctive normal level set: An efficient parametric implicit method". In: *2016 IEEE International Conference on Image Processing (ICIP)*. 2016, pp. 4299–4303. DOI: [10.1109/ICIP.2016.7533171](https://doi.org/10.1109/ICIP.2016.7533171).
- [54] Eric L Miller, Misha Kilmer, and Carey Rappaport. "A new shape-based method for object localization and characterization from scattered field data". In: *IEEE Transactions on Geoscience and Remote Sensing* 38.4 (2000), pp. 1682–1696.
- [55] Naren Naik, Rick Beatson, and Jerry Eriksson. "Radial-basis-function level-set-based regularized Gauss–Newton-filter reconstruction scheme for dynamic shape tomography". In: *Applied Optics* 53 (Oct. 2014). DOI: [10.1364/AO.53.006872](https://doi.org/10.1364/AO.53.006872).
- [56] Stanley Osher and James A Sethian. "Fronts propagating with curvature-dependent speed: Algorithms based on Hamilton-Jacobi formulations". In: *Journal of Computational Physics* 79.1 (1988), pp. 12–49. ISSN: 0021-9991. DOI: [https://doi.org/10.1016/0021-9991\(88\)90002-2](https://doi.org/10.1016/0021-9991(88)90002-2). URL: <https://www.sciencedirect.com/science/article/pii/0021999188900022>.
- [57] Stanley J. Osher and Fadil Santosa. "Level Set Methods for Optimization Problems Involving Geometry and Constraints: I. Frequencies of a Two-Density Inhomogeneous Drum". In: *Journal of Computational Physics* 171.1 (2001), pp. 272–288. ISSN: 0021-9991. DOI: <https://doi.org/10.1006/jcph.2001.6789>. URL: <https://www.sciencedirect.com/science/article/pii/S0021999101967890>.
- [58] Gad El-Qady et al. "Imaging subsurface cavities using geoelectric tomography and ground-penetrating radar". In: *Journal of cave and karst studies* 67.3 (2005), pp. 174–181.
- [59] I.T. Rekanos, T.V. Yioultsis, and T.D. Tsiboukis. "Inverse scattering using the finite-element method and a nonlinear optimization technique". In: *IEEE Trans-*

- actions on Microwave Theory and Techniques* 47.3 (1999), pp. 336–344. DOI: [10.1109/22.750236](https://doi.org/10.1109/22.750236).
- [60] S.M. Riad. “The deconvolution problem: An overview”. In: *Proceedings of the IEEE* 74.1 (1986), pp. 82–85. DOI: [10.1109/PROC.1986.13407](https://doi.org/10.1109/PROC.1986.13407).
 - [61] Arvind K. Saibaba et al. “Randomized approaches to accelerate MCMC algorithms for Bayesian inverse problems”. In: *Journal of Computational Physics* 440 (2021), p. 110391. ISSN: 0021-9991. DOI: <https://doi.org/10.1016/j.jcp.2021.110391>. URL: <https://www.sciencedirect.com/science/article/pii/S0021999121002862>.
 - [62] Christophe Samson et al. “A Level Set Model for Image Classification”. In: *International Journal of Computer Vision* 40 (Jan. 2000), pp. 187–197. DOI: [10.1023/A:1008183109594](https://doi.org/10.1023/A:1008183109594).
 - [63] Fadil Santosa. “A level-set approach for inverse problems involving obstacles”. In: *ESAIM: Control, Optimisation and Calculus of Variations* 1 (1996), pp. 17–33. DOI: [10.1051/cocv:1996101](https://doi.org/10.1051/cocv:1996101).
 - [64] O. Semerci and E. L. Miller. “A Parametric Level-Set Approach to Simultaneous Object Identification and Background Reconstruction for Dual-Energy Computed Tomography”. In: *IEEE Transactions on Image Processing* 21.5 (2012), pp. 2719–2734. DOI: [10.1109/TIP.2012.2186308](https://doi.org/10.1109/TIP.2012.2186308).
 - [65] Yanyan Shi et al. “A Non-Convex L1-Norm Penalty-Based Total Generalized Variation Model for Reconstruction of Conductivity Distribution”. In: *IEEE Sensors Journal* 20.14 (2020), pp. 8137–8146. DOI: [10.1109/JSEN.2020.2981873](https://doi.org/10.1109/JSEN.2020.2981873).
 - [66] Eric de Sturler and Misha Kilmer. “A Regularized Gauss–Newton Trust Region Approach to Imaging in Diffuse Optical Tomography”. In: *SIAM J. Scientific Computing* 33 (Jan. 2011), pp. 3057–3086. DOI: [10.1137/100798181](https://doi.org/10.1137/100798181).
 - [67] Eric de Sturler et al. “Nonlinear Parametric Inversion Using Interpolatory Model Reduction”. In: *SIAM J. Sci. Comput* 37(3) (2015), B495–B517.
 - [68] Xue-Cheng Tai and TONY CHAN. “A survey on multiple level set methods with applications for identifying piecewise constant functions”. In: *International Journal of Numerical Analysis and Modeling* 1 (Jan. 2004).
 - [69] Andrey N. Tikhonov and Vasilii Y. Arsenin. *Solutions of ill-posed problems*. Translated from the Russian, Preface by translation editor Fritz John, Scripta Series in Mathematics. Washington, D.C.: John Wiley & Sons, New York: V. H. Winston & Sons, 1977, pp. xiii+258.
 - [70] Françoise Tisseur. “Newton’s Method in Floating Point Arithmetic and Iterative Refinement of Generalized Eigenvalue Problems”. In: *SIAM Journal on Matrix Analysis and Applications* 22.4 (2001), pp. 1038–1057. DOI: [10.1137/S0895479899359837](https://doi.org/10.1137/S0895479899359837). eprint: <https://doi.org/10.1137/S0895479899359837>. URL: <https://doi.org/10.1137/S0895479899359837>.
 - [71] Bruce J Tromberg et al. “Assessing the future of diffuse optical imaging technologies for breast cancer management”. In: *Medical physics* 35.6Part1 (2008), pp. 2443–2451.
 - [72] Andy Tsai, A. Jr, and A.S. Willsky. “Curve evolution implementation of the Mumford-Shah functional for image segmentation, denoising, interpolation, and magnification”. In: *Image Processing, IEEE Transactions on* 10 (Sept. 2001), pp. 1169–1186. DOI: [10.1109/83.935033](https://doi.org/10.1109/83.935033).
 - [73] L. Vese and T. Chan. “A Multiphase Level Set Framework for Image Segmentation Using the Mumford and Shah Model”. In: *International Journal of Computer Vision* 50 (2004), pp. 271–293.

- [74] Rossmary Villegas et al. “Simultaneous Characterization of Geological Shapes and Permeability Distributions in Reservoirs Using the Level Set Method”. In: June 2006. DOI: [10.2523/100291-MS](https://doi.org/10.2523/100291-MS).
- [75] Curtis R. Vogel. *Computational Methods for Inverse Problems*. Society for Industrial and Applied Mathematics, 2002. DOI: [10.1137/1.9780898717570](https://doi.org/10.1137/1.9780898717570). eprint: <https://epubs.siam.org/doi/pdf/10.1137/1.9780898717570>. URL: <https://epubs.siam.org/doi/abs/10.1137/1.9780898717570>.
- [76] Michael Yu Wang and Xiaoming Wang. ““Color” level sets: a multi - phase method for structural topology optimization with multiple materials”. In: *Computer Methods in Applied Mechanics and Engineering* 193.6 (2004), pp. 469–496. ISSN: 0045-7825. DOI: <https://doi.org/10.1016/j.cma.2003.10.008>. URL: <https://www.sciencedirect.com/science/article/pii/S0045782503005644>.
- [77] Zhou Wang et al. “Image quality assessment: from error visibility to structural similarity”. In: *IEEE Transactions on Image Processing* 13.4 (2004), pp. 600–612. DOI: [10.1109/TIP.2003.819861](https://doi.org/10.1109/TIP.2003.819861).
- [78] Charles J Werth et al. “A review of non-invasive imaging methods and applications in contaminant hydrogeology research”. In: *Journal of contaminant hydrology* 113.1-4 (2010), pp. 1–24.
- [79] Quan Zhang et al. “Coregistered tomographic x-ray and optical breast imaging: initial results”. In: *Journal of biomedical optics* 10.2 (2005), p. 024033.
- [80] Hong-Kai Zhao et al. “A Variational Level Set Approach to Multiphase Motion”. In: *Journal of Computational Physics* 127.1 (1996), pp. 179–195. ISSN: 0021-9991. DOI: <https://doi.org/10.1006/jcph.1996.0167>. URL: <https://www.sciencedirect.com/science/article/pii/S0021999196901679>.

Appendix A. Parameter selection and experiment details.

Hyper-parameters		
Experiment	$\mu/w/c$	$\alpha(\text{TV})$
Denoising: Gaussian	10/0.05/0.01	3.2e2
Denoising: Salt and Pepper	10/0.05/0.01	1.9e1
Denoising: Poisson	10/0.05/0.01	5.5e2
Denoising: Speckle	10/0.05/0.01	4.1e2
Deconvolution	10/0.05/0.01	8.8e3
Sparse Angle Tomography	10/0.05/0.01	3.0e1
Limited View Tomography	10/0.05/0.01	3.0e1
3D Tomography	10/0.001/0.01	8.0e2
Diffuse Optical Tomography	4/0.001/0.01	-

Fig. A.1: Hyper-parameters values used for the experiments in this paper.

In this paper, for the 2D problems N^2 basis functions of PaLEnTIR formulation are centered on an equally spaced $N \times N$ grid. The initial weight parameters α_i of basis functions are sampled from a zero-mean uniform distribution with a standard deviation of 0.01, $U(-0.02, 0.02)$. The stretching parameters β_i are all initialized to 0.015 and the sliding parameters γ_i are all initialized to 0.1. The space varying contrast limits are all initialized to the maximum(for \mathbf{C}_H) and minimum(for \mathbf{C}_L) values of the overall image while using the Algorithm 3.1. The window size of max/min windows for the Algorithm (3.1) is chosen as 29×29 . Similarly, for the 3D problems, basis functions are centered on an equally spaced $N \times N \times N$ grid. The initial weight

parameters α_i of basis functions are sampled from a zero-mean uniform distribution with a standard deviation of 0.01, $U(-0.02, 0.02)$. The stretching parameters $\beta_{i,j}$ are all initialized to 0.5 and the sliding parameters $\gamma_{i,j}$ are all initialized to 0.31. The space varying contrast limits are all initialized to the maximum(for \mathbf{C}_H) and minimum(for \mathbf{C}_L) values of the overall image while using the Algorithm 3.1. The values of fixed parameters/hyper-parameters required in the experiments are shown in Table A.1. For the plots in Figure 3.6, the true image which both PaLS models were optimized to represent is shown in Figure A.2.

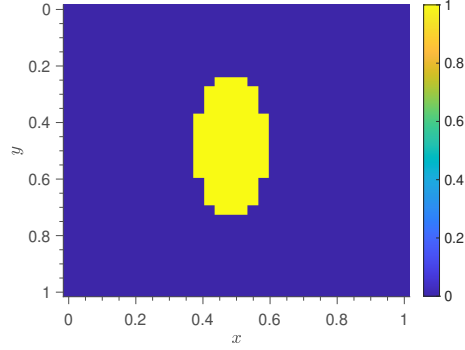


Fig. A.2: The image used to perform the experiments for Figure 3.6.

Appendix B. TREGS Settings. In this section we give details about how we used TREGS algorithm in our experiments. For more specific details about the algorithm please refer to [66]. The input of the algorithm is the initial parameter vector which was given in this paper as described in Appendix A. The algorithm requires the Jacobian matrix of the residual as well. The derivatives for Jacobian calculation are given in the following sections. We used three stopping criteria for our experiments. The first criterion is the drop of the residual decrease between two consecutive TREGS iterations below 0.001. The second stopping criterion is the drop of the residual to the level of the noise norm of the input data. The final criterion is reaching the maximum iteration number which we chose as 10000.

Appendix C. Derivatives of the PaLS with respect to model parameters. In this section we compute the derivatives of the PaLS in (2.6). The PaLS model is defined as,

$$(C.1) \quad f(\mathbf{r}; \mathbf{p}) = C_H H_\epsilon(\phi_{\text{rbf}}(\mathbf{r}; \mathbf{p})) + C_L (1 - H_\epsilon(\phi_{\text{rbf}}(\mathbf{r}; \mathbf{p})))$$

The derivative of $f(\mathbf{r}; \mathbf{p})$ with respect to a parameter p_i is written by using the chain rule as,

$$(C.2) \quad \frac{\partial f(\mathbf{r}; \mathbf{p})}{\partial p_j} = (C_H - C_L) H'_\epsilon(\phi_{\text{rbf}}(\mathbf{r}; \mathbf{p})) \frac{\partial \phi_{\text{rbf}}(\mathbf{r}; \mathbf{p})}{\partial p_j}.$$

The first term on the right side in (C.2) is simply the difference between the contrast coefficients. The second term is the derivative of the approximate Heaviside function. In this work, for a c -level set, the approximate Heaviside function is defined as,

$$(C.3) \quad H_\epsilon(x) = \frac{1}{2} \left[1 + \frac{2}{\pi} \tan^{-1} \left(\frac{\pi(x - c)}{\epsilon} \right) \right].$$

The derivative of the approximate Heaviside function is given as,

$$(C.4) \quad H'_\epsilon(\phi_{\text{rbf}}(\mathbf{r}; \mathbf{p})) = \frac{1}{\epsilon} \left[\frac{1}{1 + (\frac{\pi x}{\epsilon})^2} \right].$$

The third term in (C.2) is the derivative of the PaLS function with respect to model parameters. For the RBF PaLS, we need the derivative of ϕ_{rbf} in 2.6. The derivatives with respect to different parameters are listed as,

$$(C.5) \quad \frac{\partial \phi_{\text{rbf}}(\mathbf{r}; \mathbf{p})}{\partial \alpha_i} = \psi(\|\beta_i(\mathbf{r} - \boldsymbol{\chi}_i)\|)$$

$$(C.6) \quad \frac{\partial \phi_{\text{rbf}}(\mathbf{r}; \mathbf{p})}{\partial \beta_i} = \alpha_i \frac{\partial \psi(\|\beta_i(\mathbf{r} - \boldsymbol{\chi}_i)\|)}{\partial \beta_i}$$

$$(C.7) \quad \frac{\partial \phi_{\text{rbf}}(\mathbf{r}; \mathbf{p})}{\partial \chi_i^j} = \alpha_i \frac{\partial \psi(\|\beta_i(\mathbf{r} - \boldsymbol{\chi}_i)\|)}{\partial \chi_i^j}.$$

where χ_i^j is the j th element of center location of i th basis function $\boldsymbol{\chi}_i$. In this paper, we used basis functions, defined in (3.4), to form ψ . The derivatives of ψ with respect to β_i , χ_i^j are defined as,

$$(C.8) \quad \frac{\partial \psi(\|\beta_i(\mathbf{r} - \boldsymbol{\chi}_i)\|)}{\partial \beta_i} = -2\beta_i(\mathbf{r} - \boldsymbol{\chi}_i)^T(\mathbf{r} - \boldsymbol{\chi}_i)\psi(\|\beta_i(\mathbf{r} - \boldsymbol{\chi}_i)\|)$$

$$(C.9) \quad \frac{\partial \psi(\|\beta_i(\mathbf{r} - \boldsymbol{\chi}_i)\|)}{\partial \chi_i^j} = 2\beta_i^2(r^j - \chi_i^j)\psi(\|\beta_i(\mathbf{r} - \boldsymbol{\chi}_i)\|).$$

C.1. Derivatives of the 2D PaLEnTIR with respect to model parameters. The PaLEnTIR model can be written as

$$(C.10) \quad f(\mathbf{r}; \mathbf{p}) = C_H T_w(\phi(\mathbf{r}; \mathbf{p})) + C_L (1 - T_w(\phi(\mathbf{r}; \mathbf{p}))).$$

The derivative of $f(\mathbf{r}; \mathbf{p})$ with respect to a parameter p_i is written by using the chain rule as,

$$(C.11) \quad \frac{\partial f(\mathbf{r}; \mathbf{p})}{\partial p_j} = (C_H - C_L) T'_w(\phi(\mathbf{r}; \mathbf{p})) \frac{\partial \phi(\mathbf{r}; \mathbf{p})}{\partial p_j}.$$

The transition function has the same definition as of the approximate Heaviside function except we replace ϵ with w . The same holds for the derivative of the transition function.

Similar to the RBF PaLS, the third term is the derivative of the PaLEnTIR function with respect to model parameters. We need the derivatives of ϕ which is defined in 3.2. The derivatives with respect to different parameters are listed as,

$$(C.12) \quad \frac{\partial \phi(\mathbf{r}; \mathbf{p})}{\partial \alpha_i} = \frac{\partial \sigma_h(\alpha_i)}{\partial \alpha_i} \psi(\mathbf{R}_j(\mathbf{r} - \boldsymbol{\chi}_j))$$

$$(C.13) \quad \frac{\partial \phi(\mathbf{r}; \mathbf{p})}{\partial \beta_i} = \sigma_h(\alpha_i) \frac{\partial \psi(\mathbf{R}_j(\mathbf{r} - \boldsymbol{\chi}_j))}{\partial \beta_i}$$

$$(C.14) \quad \frac{\partial \phi(\mathbf{r}; \mathbf{p})}{\partial \gamma_i} = \sigma_h(\alpha_i) \frac{\partial \psi(\mathbf{R}_j(\mathbf{r} - \boldsymbol{\chi}_j))}{\partial \gamma}.$$

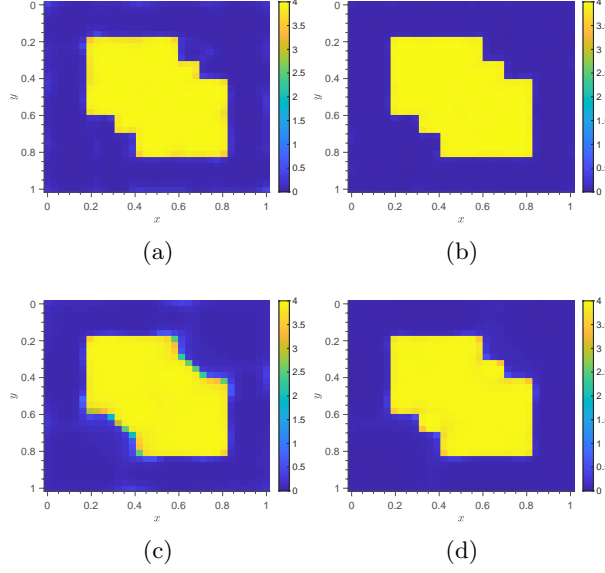


Fig. C.1: (a)PaLEnTIR recovery using 5×5 ABFs. (b)PaLEnTIR recovery using 6×6 ABFs. (c)PaLS recovery using 6×6 RBFs. (d) PaLS recovery using 7×7 RBFs

The derivatives with respect to parameters required in equations above are defined as,

$$(C.15) \quad \frac{\partial \sigma_h(\alpha)}{\partial \alpha} = \frac{1}{2} \text{sech}^2\left(\frac{\alpha}{2}\right)$$

$$(C.16) \quad \frac{\partial \psi(\mathbf{R}_j(\mathbf{r} - \boldsymbol{\chi}_j))}{\partial \beta_i} = (-2\mu^2)\psi(\mathbf{R}_j(\mathbf{r} - \boldsymbol{\chi}_j))(\mathbf{r} - \boldsymbol{\chi}_j)^T \begin{bmatrix} e^{2\beta} & 0 \\ \gamma e^\beta & -e^{-\beta} \end{bmatrix} (\mathbf{r} - \boldsymbol{\chi}_j)$$

$$(C.17) \quad \frac{\partial \psi(\mathbf{R}_j(\mathbf{r} - \boldsymbol{\chi}_j))}{\partial \gamma_i} = (-\mu^2)\psi(\mathbf{R}_j(\mathbf{r} - \boldsymbol{\chi}_j))(\mathbf{r} - \boldsymbol{\chi}_j)^T \begin{bmatrix} 0 & e^\beta \\ e^\beta & 2\gamma \end{bmatrix} (\mathbf{r} - \boldsymbol{\chi}_j).$$

C.2. Visual Illustration of Shape Expressiveness. To compare the proposed ABFs with RBFs on a complicated problem, the PaLEnTIR and RBF PaLS representations of an object containing sharp and flat parts are shown in Figure C.1. Similar to section 3.1, the forward model is the identity and \mathbf{w} is vector of independent identically distributed Gaussian random variables common variance such the the signal to noise ratio is 40 dB. The images in Figure C.1a and C.1b show the PaLEnTIR representations of the object. The image in Figure C.1a is reconstructed in a uniform 5×5 grid of ABFs and has a PSNR of 32.53 dB. The sharp and flat regions of the object are perfectly captured and it is almost piecewise constant with virtually undetectable inhomogeneities. By increasing the number of ABFs to only 6×6 , we can produce an approximation that looks to the eye to be a perfect representation with an excellent PSNR of almost 39 dB. The images in Figure C.1c and C.1d show the RBF PaLS representations of the object. The image in Figure C.1c shows the PaLS representation with 6×6 RBFs. The model is able to capture the long flat regions of the object, but the small sharp regions are not captured although we use 6×6 RBFs. When we increase the RBFs to 7×7 , in Figure C.1d the model is capable

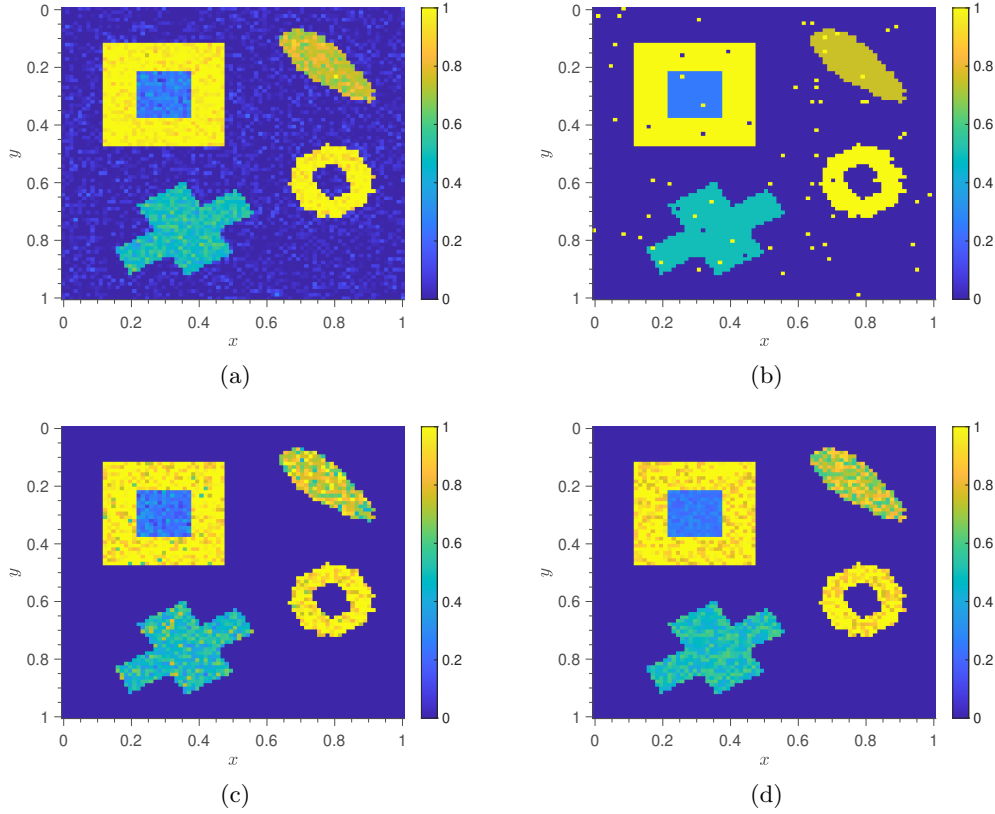
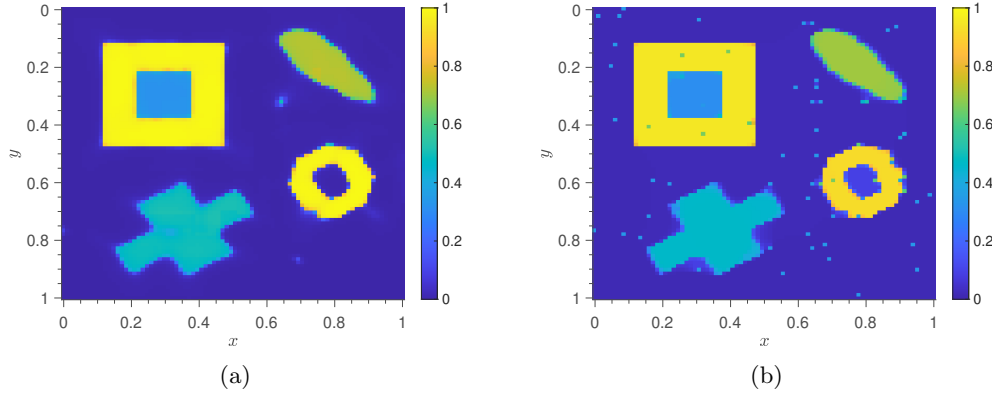


Fig. C.2: Input images, that are exposed to different types of noise, for the denoising experiment are shown. (a) Gaussian noise (b) Salt and pepper noise (c) Poisson noise (d) Speckle noise.

of capturing the sharp regions as well. As a result, by using the new basis function formulation the model is able to produce the object with a PSNR higher than 30 dB with only 25 RBFs whereas it requires 49, almost the double, with the RBF PaLS.

C.3. Denoising Experiments. In this paper, we carried out the experiment with four types of randomness: additive Gaussian noise, salt and pepper noise, multiplicative speckle, and using the true object to generate Poisson data. The resulting data are shown in Figure C.2. In this section, we will discuss the results for the denoising experiments for salt and pepper, speckle and Poisson cases.

C.3.1. Salt and Pepper. The image corrupted by salt and pepper noise is shown in Figure C.2b. The data SNR of the input is 12.99 dB. The L2-TV and the PaLenTIR reconstructions of the image and the table of performance metrics are shown in Figure C.3. From Figure C.3a, we observe that PaLenTIR managed to eliminate almost all the pixels flipped by the salt and pepper process and the reconstructed objects look homogeneous. On the other hand, the L2-TV approach passes a far larger number of the pixels flipped by the salt and pepper process. Also the contrasts of the doughnut-shaped object is less accurately recovered for the L2-



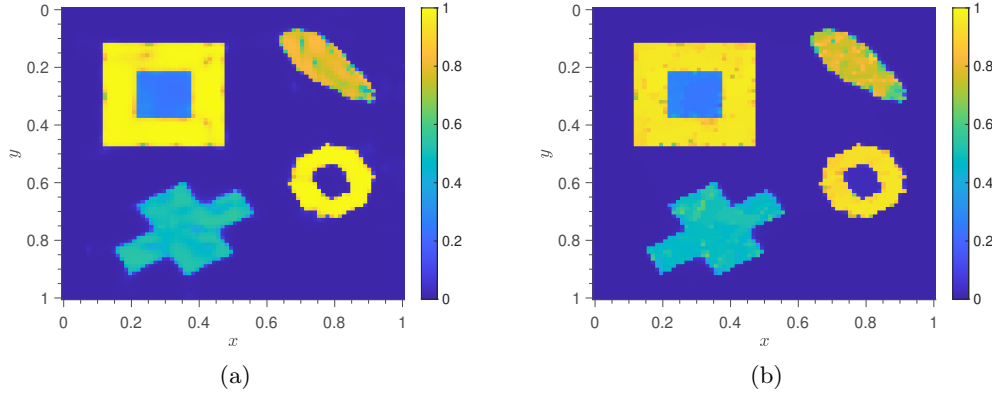
Performance Metrics of the Denoising Experiment with Salt and Pepper Noise					
Method	Unknowns	PSNR	SNR	SSIM	MSE
Total Variation	6724	24.85	17.26	0.53	3.3e-03
PaLEnTIR	432	27.44	19.85	0.90	1.8e-03

Fig. C.3: (a) PaLEnTIR reconstruction and (b) L2-TV reconstruction for the salt and pepper denoising problem. The table shows the performance metrics for both methods. The better scores are written with bold letters.

TV case compared to PaLEnTIR. These differences are reflected in the performance table in Figure C.3, where PaLEnTIR outperforms L2-TV reconstruction in all four cases. The MSE of the PaLEnTIR reconstruction is almost the half that of L2-TV while the PaLEnTIR SSIM is a factor 1.7 greater than L2-TV which suggests that the PaLEnTIR reconstruction is much better both in terms of visual goodness and absolute error. Both the PSNR and SNR values of PaLEnTIR reconstructions exceed L2-TV by more than 2 dB.

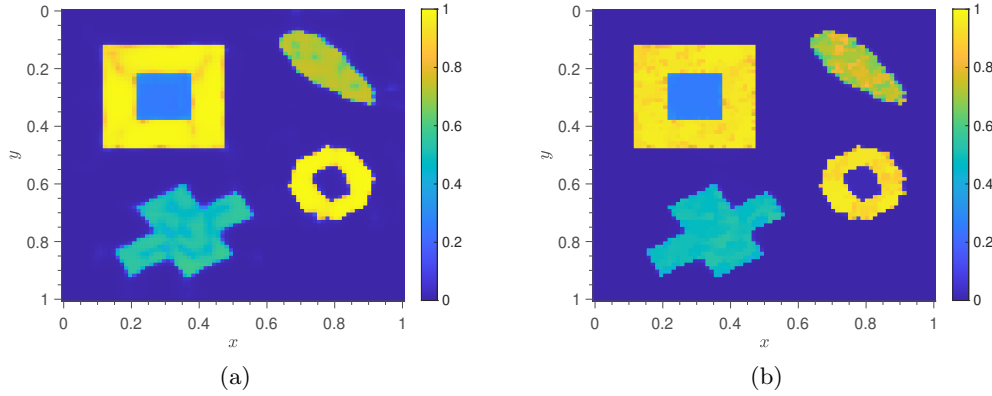
C.3.2. Poisson. The Poisson input image is shown in Figure C.2c. The data SNR of the input is 17.85 dB. The L2-TV and the PaLEnTIR reconstructions of the image and the table of performance metrics are shown in Figure C.4. The L2-TV reconstruction is strongly effected from the Poisson noise as it fails to recover the true contrast of the lower parts of the rotated ellipsoidal shape located at the upper right corner of the image. The artifacts on the objects reconstructed with the L2-TV approach are more pronounced visually. Again PaLEnTIR does well in terms of the four performance metrics.

C.3.3. Speckle. The speckle input image is shown in Figure C.2d. The SNR of the input is 19.40 dB. The L2-TV and the PaLEnTIR reconstructions of the image and the table of performance metrics are shown in Figure C.5. The object on the top right corner looks very rough in the L2-TV reconstruction. The same issue is also observed in the yellow objects. Except for the object on the bottom left corner, the other three objects look more homogeneous in the PaLEnTIR reconstruction. We note that the PaLEnTIR artifacts are fewer and smoother compared to the numerous, small discrete artifacts seen in the L2-TV reconstruction. The SSIM scores indicate that both reconstructions are visually good with the L2-TV approach slightly outperforming PaLEnTIR. The PaLEnTIR reconstruction has slightly better PSNR and



Performance Metrics of the Denoising Experiment with Poisson Noise					
Method	Unknowns	PSNR	SNR	SSIM	MSE
Total Variation	6724	28.34	20.75	0.92	1.5e-03
PaLEnTIR	432	29.78	22.19	0.95	1.1e-03

Fig. C.4: (a) PaLEnTIR reconstruction and (b) L2-TV reconstruction for the Poisson denoising problem. The table shows the performance metrics for both methods. The better scores are written with bold letters.



Performance Metrics of the Denoising Experiment with Speckle Noise					
Method	Unknowns	PSNR	SNR	SSIM	MSE
Total Variation	6724	29.62	22.03	0.95	1.1e-03
PaLEnTIR	432	29.63	22.04	0.94	1.1e-03

Fig. C.5: (a) PaLEnTIR reconstruction and (b) L2-TV reconstruction for the speckle denoising problem. The table shows the performance metrics for both methods. The better scores are written with bold letters.

SNR values whereas both approach show comparable performance in terms of MSE.